LAWRENCE
LIVERMORE
NATIONAL
LABORATORY

LLNL-JRNL-870480

On Finding Black Holes in Photometric Microlensing Surveys

Z. Kaczmarek, P. McGill, S. E. Perkins, W. A. Dawson, M. Huston, M. F. Ho, N. S. Abrams, J. R. Lu

October 12, 2024

The Astrophysical Journal

Disclaimer

The Astrophysical Journal, 981:183 (15pp), 2025 March 10 https://doi.org/10.3847/1538-4357/adb1d7

On Finding Black Holes in Photometric Microlensing Surveys

Zofia Kaczmarek[1,2], Peter McGill[1], Scott E. Perkins[1], William A. Dawson[1], Macy Huston[3], Ming-Feng Ho[4,5,6], Natasha S. Abrams[3], and Jessica R. Lu[3]
[1] Space Science Institute, Lawrence Livermore National Laboratory, 7000 East Ave., Livermore, CA 94550, USA; zofia.kaczmarek@uni-heidelberg.de, mcgill5@llnl.gov
[2] Zentrum für Astronomie der Universität Heidelberg, Astronomisches Rechen-Institut, Mönchhofstr. 12-14, 69120 Heidelberg, Germany
[3] University of California, Berkeley, Astronomy Department, Berkeley, CA 94720, USA
[4] Department of Physics and Astronomy, University of California, Riverside, 900 University Avenue, Riverside, CA 92521, USA
[5] Department of Physics, University of Michigan, 450 Church St, Ann Arbor, MI 48109, USA
[6] Leinweber Center for Theoretical Physics, 450 Church St, Ann Arbor, MI 48109, USA
Received 2024 October 17; revised 2025 January 10; accepted 2025 January 21; published 2025 March 7

Abstract

There are expected to be millions of isolated black holes in the galaxy resulting from the deaths of massive stars. Measuring the abundance and properties of this remnant population would shed light on the end stages of stellar evolution and the evolution paths of black hole systems. Detecting isolated black holes is currently only possible via gravitational microlensing, which has so far yielded one definitive detection. The difficulty in finding microlensing black holes lies in having to choose a small subset of events, based on characteristics of their light curves, to allocate expensive and scarce follow-up resources to confirm the identity of the lens. Current methods either rely on simple cuts in parameter space without using the full distribution information or are only effective on small subsets of events. In this paper, we present a new lens classification method. The classifier takes in posterior constraints on light-curve parameters and combines them with a Galactic simulation to estimate the lens class probability. This method is flexible and can be used with any set of microlensing light-curve parameters, making it applicable to large samples of events. We make this classification framework available via the `popclass` Python package. We apply the classifier to ∼10,000 microlensing events from the Optical Gravitational Lensing Experiment survey and find 23 high-probability black hole candidates. Our classifier also suggests that the only known isolated black hole is an observational outlier, according to current Galactic models, and the allocation of astrometric follow-up on this event was a high-risk strategy.

Unified Astronomy Thesaurus concepts: Gravitational microlensing (672); Black holes (162); Bayesian statistics (1900); Classification (1907); Sky surveys (1464)

Materials only available in the online version of record: machine-readable table

1. Introduction

Gravitational microlensing is sensitive to both luminous and dark objects, making it a powerful tool for studying a variety of Galactic populations (from exoplanets—e.g., Y. H. Ryu et al. 2018; to white dwarfs (WDs)—e.g., K. C. Sahu et al. 2017; P. McGill et al. 2018, 2023; to black holes—e.g., J. R. Lu et al. 2016; C. Y. Lam et al. 2022a; K. C. Sahu et al. 2022; C. Y. Lam & J. R. Lu 2023; and stars—e.g., J. Klüter et al. 2020; P. McGill et al. 2020). Microlensing's broad power has been realized in the era of modern variability surveys such as the Optical Gravitational Lensing Experiment (OGLE; A. Udalski et al. 2015), the Microlensing Observations in Astrophysics (MOA) survey (J. B. Hearnshaw et al. 2006; T. Sumi et al. 2013), the Korea Microlensing Telescope Network (S. L. Kim et al. 2016), and the VISTA Variables in the Via Lactea survey (D. Minniti et al. 2010), which have provided databases containing on the order of 10,000 microlensing events (e.g., P. Mróz et al. 2020; A. Husseiniova et al. 2021; I. G. Shin et al. 2024). This yield of events is only set to increase with the advent of the Roman Space Telescope (M. T. Penny et al. 2019; S. A. Johnson et al. 2020), unlocking high Galactic bulge event rates in the near-infrared (e.g., A. Gould 1994; Y. Shvartzvald et al. 2017; P. McGill et al. 2019; Z. Kaczmarek et al. 2024), and the Vera C. Rubin Observatory (Ž. Ivezić et al. 2019; N. S. Abrams et al. 2025b).

One of the promised strengths of microlensing is its unique sensitivity to dark and isolated objects, specifically the expected population of stellar-origin black holes (SOBHs) in the Galaxy (e.g., E. Agol et al. 2002; S. Mao et al. 2002). As SOBHs are the terminal evolutionary state of massive stars, the Milky Way is expected to contain 10^8–10^9 of them (E. Agol & M. Kamionkowski 2002). Despite this large expected abundance, only ∼50 SOBHs are known, the majority of which reside in X-ray binaries (e.g., C. T. Bolton 1972; B. L. Webster & P. Murdin 1972; J. E. McClintock & R. A. Remillard 2006; R. A. Remillard & J. E. McClintock 2006), with others in astrometric or spectroscopic binaries (K. El-Badry et al. 2023a, 2023b; Gaia Collaboration et al. 2024). In addition to the known Galactic population of SOBHs, $\sim 10^2$ extragalactic black holes, spanning masses from 2 to $200 M_\odot$, have been observed in binary black hole or neutron star (NS)–black hole mergers causing gravitational waves (B. P. Abbott et al. 2016, 2019; R. Abbott et al. 2021, 2023, 2024; M. F. Ho et al. 2024). However, all current black hole detection methods, apart from microlensing, are only sensitive to black holes in multiple systems.

Compiling a data set of isolated SOBHs detected via microlensing would enable investigations of SOBHs beyond

the current sample that followed an evolutionary path resulting in a stable binary system. A sample of isolated SOBHs could answer open questions, such as if the Galactic and extragalactic mass spectra of dark remnants are similar or whether the mass gap observed between NSs and black holes results from observational biases (e.g., Ł. Wyrzykowski & I. Mandel 2020) or an astrophysical mechanism (e.g., W. M. Farr et al. 2011; K. Belczynski et al. 2012; L. Kreidberg et al. 2012; Y. Shao 2022; R. Abbott et al. 2023; E. D. Barr et al. 2024).

The first and only current detection of an isolated black hole was recently reported via microlensing event OGLE-2011-BLG-0462/MOA-2011-BLG-191 (C. Y. Lam et al. 2022a; K. C. Sahu et al. 2022; C. Y. Lam & J. R. Lu 2023). However, determining that the lens of this event was a black hole was not straightforward. This difficulty arises because the photometric microlensing signal is degenerate in lens–source physical parameters. On the contrary, an astrometric microlensing signal not only allows us to distinguish between degenerate solutions for the source–lens trajectory (e.g., K. A. Rybicki et al. 2018), but also provides a direct measurement of the angular event scale $\theta_{\rm E}$—the "missing ingredient" for determining the lens mass (E. Hog et al. 1995; M. Miyamoto & Y. Yoshii 1995; M. A. Walker 1995). Therefore, astrometric follow-up from the Hubble Space Telescope was required to confidently identify the lens as a black hole. In this common scenario, using parameters extracted from photometry (in this case, primarily the timescale of $\gtrsim$200 days; K. C. Sahu et al. 2022), the lens had to be identified as a likely black hole candidate beforehand —to justify the use of expensive follow-up observations to confirm its nature.

Even in the upcoming era of multiple space-based submilliarcsecond-capable observatories (e.g., the James Webb Space Telescope—J. P. Gardner et al. 2006; the Roman Space Telescope—D. Spergel et al. 2015; and Gaia—Gaia Collaboration et al. 2016), the majority of microlensing events will only be detected photometrically in the first instance. Therefore, determining if a given event is caused by a black hole based on only photometric signals remains critical to efficiently allocating expensive follow-up resources (e.g., further photometric or astrometric observations via adaptive optics—S. K. Terry et al. 2022; interferometry—S. Dong et al. 2019; or late-time high-resolution imaging—F. N. Abdurrahman et al. 2021) to increase the yield of detected isolated black holes.

Microlensing occurs when an intervening massive object gravitationally deflects and magnifies the light from a more distant background source. For the majority of microlensing events, the only information is available from the light curve that traces the physical parameters of the lens and is almost always well constrained in the Einstein timescale of the event:

$$t_{\rm E} = \frac{D_L \theta_{\rm E}}{v_{\rm rel}}. \tag{1}$$

Here, $v_{\rm rel}$ is the relative len–-source transverse velocity, D_L is the distance to the lens, and $t_{\rm E}$ is the time it takes to cross the angular Einstein radius of the system, $\theta_{\rm E} = \sqrt{4GM_L c^{-2}(D_L^{-1} - D_S^{-1})}$, where M_L is the mass of the lens and D_S is the distance to the source.

For some events, the imprint of Earth's orbital acceleration can be detected as an asymmetrical imprint on the microlensing light curve (e.g., Ł. Wyrzykowski et al. 2015; Z. Kaczmarek et al. 2022), allowing the microlensing parallax,

$$\pi_{\rm E} = \frac{1\ {\rm au}}{\theta_{\rm E}}\left(\frac{1}{D_L} - \frac{1}{D_S}\right), \tag{2}$$

to be well constrained. For events without a clear parallax signal, upper limits can be placed on $\pi_{\rm E}$ (e.g., N. Golovich et al. 2022). However, these parameters alone are not sufficient to directly determine the lens mass and identify the nature of the lens, due to various degeneracies (e.g., M. C. Smith et al. 2003; A. Gould 2004).

To overcome this challenge, Galactic and stellar models can be used in combination with microlensing light-curve constraints to infer the missing physical parameters of the lens (e.g., D. P. Bennett et al. 2002; S. Poindexter et al. 2005; M. C. Smith et al. 2005; Ł. Wyrzykowski et al. 2016; F. N. Abdurrahman et al. 2021). The state-of-the-art implementations of lens parameter inference using Galactic/stellar models are detailed in K. Howil et al. (2025) and E. Bachelet et al. (2024) and implemented in the `DarkLensCode`[7] and `pyLIMASS` Python packages, respectively. `DarkLensCode` has been applied to samples of events with large parallax signals and has found many promising black hole candidates (Ł. Wyrzykowski et al. 2016; Z. Kaczmarek et al. 2022; K. Kruszyńska et al. 2024; K. A. Rybicki et al. 2024). `pyLIMASS` can use observables from different channels (multiband photometry, spectroscopy, and astrometry) for a given microlensing event and combines them with stellar models in the form of isochrones; `pyLIMASS` recovers lens masses with a median precision of 20% over a simulated Roman data set (E. Bachelet et al. 2024).

`DarkLensCode` is designed to find black hole lenses, and it works by leveraging a nonzero constraint on $\pi_{\rm E}$ along with a source proper-motion estimate to constrain the lens motion, which is a crucial input for a Galactic phase-space density model. `DarkLensCode` uses this information in combination with the fraction of blended light in the event to derive lens mass and distance estimates along with the probability that the lens is dark, i.e., the probability that the fraction of blended light cannot be explained by a stellar lens at a consistent distance. While this approach proves effective for events with a nearby lens, large parallax signal, and auxiliary proper-motion information, it is not designed to classify the majority of events that do not have these characteristics.

In this work, we develop a complementary method to that of K. Howil et al. (2025) for finding black hole lenses, which fills the gap in microlensing dark remnant searches and classifications. We build a Bayesian classifier that takes posterior samples from light-curve event modeling as inputs and returns the probability of the event belonging to a given astrophysical class, given a Galactic model. This classification method is flexible and can be used with any Monte Carlo simulation of the Galaxy, permitting straightforward ways of testing the effects of different Galactic model assumptions on lens classification. The classifier does not require auxiliary information, such as source astrometry, and it can be used in weak parallax regimes, where most SOBH lenses are expected to reside (e.g., C. Y. Lam et al. 2020). Overall, this means the classifier can be quickly and uniformly applied to entire catalogs of photometric microlensing events.

[7] https://github.com/BHTOM-Team/DarkLensCode

The paper is structured as follows. In Section 2, we describe the data used in this work, comprising posterior samples from N. Golovich et al. (2022) of parameters of ∼10,000 OGLE-III and OGLE-IV microlensing events (Ł. Wyrzykowski et al. 2015; P. Mróz et al. 2019). In Section 3, we detail our lens classification method. In particular, we describe the specific Galactic simulations used by the classifier and detail the classification procedure, based on Bayesian statistics. In Section 4, we present the classification results. In particular, we compare classifications with different underlying initial–final mass relations (IFMRs), present a sample of 23 high-probability black hole candidates, and outline a fast method of approximating $p(\text{SOBH}|\boldsymbol{d}, \mathcal{G})$, the probability of the lens belonging to the SOBH class (given the data collected for the lensing event $\boldsymbol{d}$ and the Galactic model $\mathcal{G}$). We also discuss the candidates in detail, including their expected astrometric signals. Finally, in Section 6, we discuss and summarize the implications of this work for upcoming surveys such as the Vera C. Rubin Observatory and the Roman Space Telescope.

2. Data

We use the data set of publicly available microlensing events from OGLE-III (A. Udalski 2003) and OGLE-IV (A. Udalski et al. 2015) detected toward the Galactic bulge. The OGLE-III and OGLE-IV surveys were conducted at the 1.3 m Warsaw University Telescope, Las Campanas Observatory, in Chile, between 2002–2009 and 2010–2017, respectively. Specifically, we use the set of 3560 microlensing events found by Ł. Wyrzykowski et al. (2015) and the set of 5790 low-cadence field events in P. Mróz et al. (2019).[8] For this total set of 9350 events, we use the posterior distributions of microlensing event parameters obtained in N. Golovich et al. (2022). N. Golovich et al. (2022) simultaneously modeled the microlensing parallax, systematic instrumental effects, and source variability to obtain posterior distributions that minimized bias in the physical parameters of the events.

3. Bayesian Lens Classification

3.1. Galactic Model

For the model of the galaxy and simulation of microlensing events, $\mathcal{G}$, we use the Population Synthesis Code for Compact Object Microlensing Events (`PopSyCLE`; C. Y. Lam et al. 2020). The underlying stellar population in `PopSyCLE` uses the the Besançon model (A. C. Robin et al. 2004) implemented by `Galaxia` (S. Sharma et al. 2011). In this simulation, SOBHs, NSs, and WDs are generated by evolving clusters matching thin- and thick-disk, bulge, and stellar halo stellar populations in `Galaxia` via the Stellar Population Interface for Stellar Evolution and Atmospheres code (`SPISEA`; M. W. Hosek et al. 2020).

`PopSyCLE` breaks up the `Galaxia` population into age and metallicity bins, and `SPISEA` generates single-age, single-metallicity, and single-initial-mass-function (IMF) clusters to match the binned distributions. `SPISEA` uses an IMF, stellar multiplicity, extinction law, metallicity-dependent stellar evolution, and separate IFMRs for SOBHs, NSs, and WDs (J. S. Kalirai et al. 2008; C. Y. Lam et al. 2020). Finally, SOBHs and NSs are given initial progenitor kick velocities. All the values and relationships adopted for our simulations are in Table 1. For this study, we explore Galactic models with three different IFMRs (M. Spera et al. 2015; T. Sukhbold et al. 2016; C. A. Raithel et al. 2018), because this is likely to affect the predictions for SOBHs in our classification framework (S. Rose et al. 2022). Hereafter, we use the T. Sukhbold et al. (2016) IFMR as the default choice of model (e.g., for visualization), as it is the most updated with recent results and includes both metallicity dependence and explosion physics. Still, we report classification results with all IFMRs, and we consider all IFMRs equally for black hole candidate selection.

To generate a representative sample of microlensing events, we ran the Galactic simulation over 20 different locations across the OGLE bulge fields, with an area of 0.3 $\deg^2$ each (see Table 4 in Appendix B). Microlensing events are selected from this simulation by selecting lens–source pairs that come within θ_E separation of each other and have a source I-band baseline magnitude <21. We note that OGLE survey selection functions (e.g., the t_E selection efficiency) do not need to be included when calculating the class of single microlensing events—see Section 3.2 of S. E. Perkins et al. (2024) for a derivation of this point.

3.2. Classification Procedure

From the Galactic simulation, we have a simulated catalog of events labeled by lens type, with predicted distributions in the space of microlensing light-curve parameters. Figure 1 shows the simulated catalog of events in the $t_E - \pi_E$ space separated by lens class: star, WD, NS, or SOBH. We can see that events with different lens classes lie in different but overlapping regions of this space, making it useful for classifying events. In Figure 1 and the work that follows, we use a kernel density estimate (KDE) via `scipy` (P. Virtanen et al. 2020), with a bandwidth determined using Scott's rule (D. W. Scott 1992), to calculate the probability density functions for each lens class in all microlensing parameters.

Following S. E. Perkins et al. (2024), we can leverage these simulation predictions from the model of the Galaxy to classify the lens of a given event. We can calculate the probability that a microlensing event has a particular class given its light-curve data, $\boldsymbol{d}$, and the Galactic model, $\mathcal{G}$:

$$p(\text{class}_L|\boldsymbol{d}, \mathcal{G}) = \frac{p(\text{class}_L|\mathcal{G})p(\boldsymbol{d}|\text{class}_L, \mathcal{G})}{p(\boldsymbol{d}|\mathcal{G})}, \tag{3}$$

where $\text{class}_L \in \{\text{Star, WD, NS, SOBH}\}$ denotes the lens class. We can now write Equation (3) in a form that can be computed by introducing parameters of the microlensing light curve $\phi = [t_E, \pi_E, ...]$:

$$p(\text{class}_L|\boldsymbol{d}, \mathcal{G}) = \frac{p(\text{class}_L|\mathcal{G})}{p(\boldsymbol{d}|\mathcal{G})} \int p(\boldsymbol{d}|\phi)p(\phi|\text{class}_L, \mathcal{G})d\phi. \tag{4}$$

The integral can then be approximated via an importance-sampling approximation, using S independent posterior samples, ϕ_c, obtained by fitting the light curve, $\boldsymbol{d}$, under some prior $\pi(\phi)$:

$$\int p(\boldsymbol{d}|\phi)p(\phi|\text{class}_L, \mathcal{G})d\phi \approx \frac{1}{S}\sum_{c=0}^{S} \frac{p(\phi_c|\text{class}_L, \mathcal{G})}{\pi(\phi_c)}. \tag{5}$$

[8] We omit the high-cadence field data from P. Mróz et al. (2019), due to these data not being publicly available.

Table 1
PopSyCLE Simulation Parameters

Parameter	Value
Milky Way escape velocity	550 km s^{-1} (T. Piffl et al. 2014)
Sun–Galactic center distance	8.3kpc
Peak of initial SOBH progenitor kick distribution	100 km s^{-1}
Peak of initial NS progenitor kick distribution	350 km s^{-1}
IFMR	(M. Spera et al. 2015; T. Sukhbold et al. 2016; C. A. Raithel et al. 2018)
Extinction law	(A. Damineli et al. 2016)
Bar dimensions (radius, major axis, minor axis, and height)	(2.54, 0.70, 0.424, 0.424) kpc
Bar angle (Sun–Galactic center, second, and third)	(62.0, 3.5, 91.3)°
Bulge velocity dispersion (radial, azimuthal, and z)	(100, 100, 100) km s^{-1}
Bar pattern speed	40.00 km s^{-1} kpc^{-1}
Multiplicity	Singles

Note. The implementation of the IFMR is described in detail in S. Rose et al. (2022). Galactic parameters are consistent with "v3" in C. Y. Lam et al. (2020, Appendix A), and match the event rates reported by OGLE (P. Mróz et al. 2019). We investigate three different options for the IFMRs.

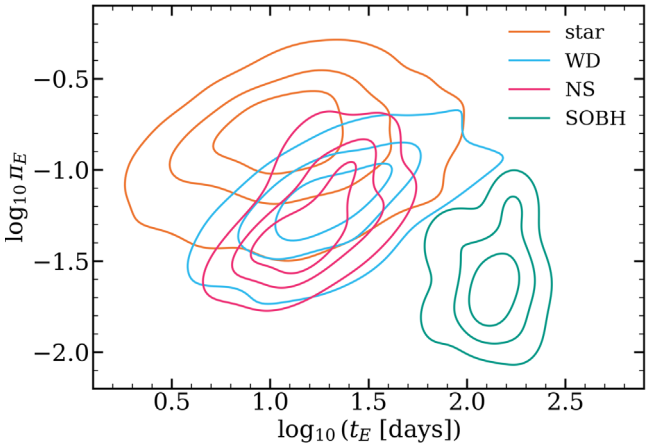

Figure 1. Simulation of microlensing events using the Galactic model parameters in Table 1 and the T. Sukhbold et al. (2016) IFMR projected into $\log_{10}t_E$–$\log_{10}\pi_E$ space. Events with different lens classes occupy different but overlapping regions of this space. The contours enclose 30%, 60%, and 90% of the probability mass for each class and were calculated using KDEs of the simulated catalog of events.

Here, $p(\phi_c|\text{class}_L, \mathcal{G})$ is calculated by using the Galactic-model-class KDE estimate seen in Figure 1, and $\pi(\phi)$ must have support over the class KDE for the importance-sampling approximation to be reliable.

In Equation (4), $p(\text{class}_L|\mathcal{G})$ is the fraction of events that have class_L in the Galactic model, $\mathcal{G}$. Assuming that our set of considered lens classes is complete, the evidence of a single lens (the denominator of Equation (4)) is

$$p(\boldsymbol{d}|\mathcal{G}) = \sum_{\text{class}_L \in \text{classes}} p(\text{class}_L|\mathcal{G})\, p(\boldsymbol{d}|\text{class}_L, \mathcal{G}), \quad (6)$$

which normalizes the class probabilities to unity. In this work, we choose to link $\mathcal{G}$ to the lens classification using the subset of microlensing light-curve parameters $\phi \equiv [\log_{10}t_E, \log_{10}\pi_E]$, which has been demonstrated to be an effective space for delineating lens classes (e.g., C. Y. Lam et al. 2020; N. Golovich et al. 2022; J. Fardeen et al. 2024; S. E. Perkins et al. 2024; K. Pruett et al. 2024). Choosing a subset of the event parameters to link $\mathcal{G}$ to the lens class is an approximation, and this classifier could in principle be used with any subset of parameters or the complete set. In this work, we choose $\phi \equiv [\log_{10}t_E, \log_{10}\pi_E]$, because this space shows intrinsic separation in lens class, can be constrained from the event light curve, and the KDEs are relatively robust and fast to construct in two dimensions.

3.3. Epistemic Uncertainty of the Galactic Model

Galactic models that produce Monte Carlo simulations of microlensing events can be incomplete in two main ways. First, they can simply be incomplete in their lens populations. For example, the PopSyCLE simulation used in this work does not contain substellar lenses below $0.07M_\odot$ (C. Y. Lam et al. 2020), such as brown dwarfs or free-floating planets (e.g., S. A. Johnson et al. 2020). Second, Monte Carlo simulations can be noisy and incomplete in the tails of the event parameter distributions, especially given the computational cost of microlensing simulations.

Over the course of developing the classifier, we encountered issues with the noisy tails of the simulation-class KDEs in the $\log_{10}t_E - \log_{10}\pi_E$ space, related to the second aforementioned problem. For example, despite the WD and NS distributions being nested in the wings of a far more numerous and dominant star distribution (see Figure 1)—so the probability of a WD or NS lens should be $\ll 1.0$—the classifier predicted $p(\text{class}_L|\boldsymbol{d}, \mathcal{G}) \sim 1.0$ for $\text{class}_L \in$ (WD, NS) for some events. In these cases, the events in question had posterior distributions with many samples in regions of $\log_{10}t_E - \log_{10}\pi_E$ that had little or no simulation support from the Galactic simulation. In turn, this caused the KDE estimates of the WD and NS classes to be extrapolated and evaluated in their noisy tails well beyond any simulation support.

To remedy this issue, we introduced an additional "None" class that has nonzero density in regions of $\log_{10}t_E - \log_{10}\pi_E$ that do not have any samples from the Galactic model for any class. To construct the probability density for this class, we define a grid of 1000×1000 bins over the entire $\log_{10}t_E$–$\log_{10}\pi_E$ subspace allowed by the priors used in the event modeling ($0.5\ \text{days} < t_E < 3000\ \text{days}$, $10^{-5} < \pi_E < 3$). We evaluate the density of a 2D KDE constructed using the positions of all simulated events, $p(\phi|\mathcal{G})$. We use a top-hat KDE implemented in `scikit-learn` (F. Pedregosa et al. 2011) for a sharp slope between covered and uncovered regions, with a bandwidth of 0.4, chosen to be minimal while still returning a simply connected space of nonzero values over the bulk of the $\log_{10}t_E$–$\log_{10}\pi_E$ space. We then assign values p

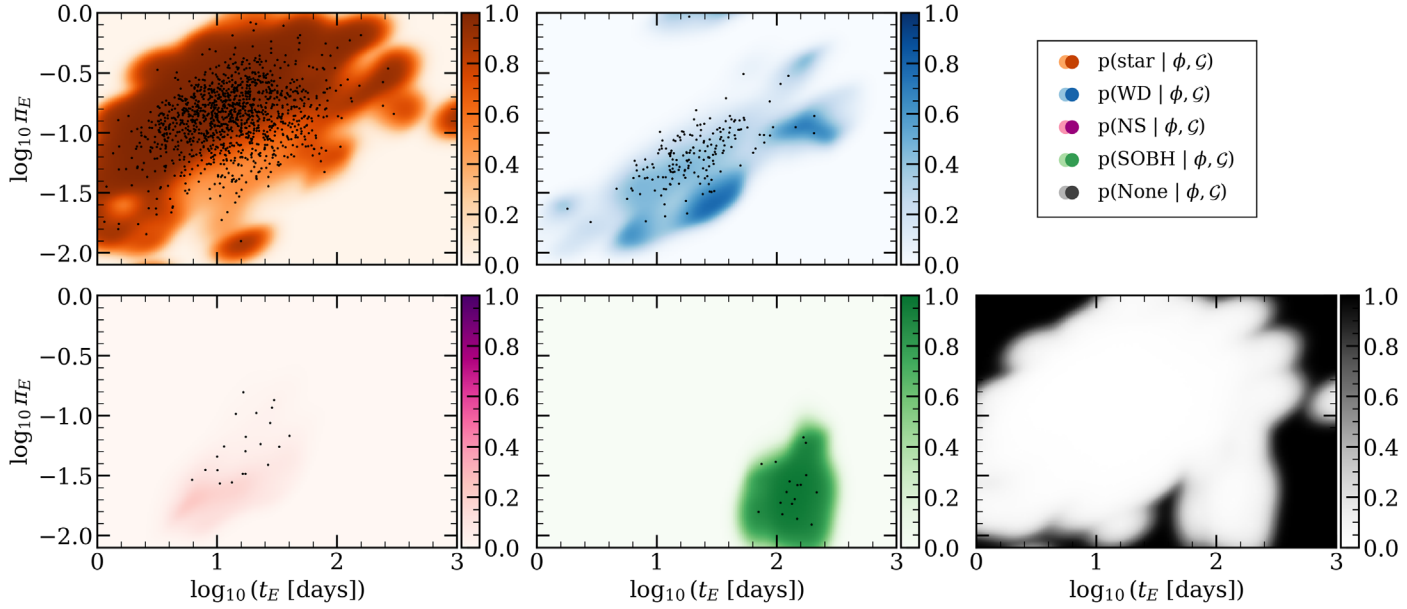

Figure 2. Relative lens classification probabilities in $\log_{10}t_{\rm E}$–$\log_{10}\pi_{\rm E}$ space for the `PoPSyCLE` model detailed in Table 1 with the T. Sukhbold et al. (2016) IFMR, evaluated on a 1000 × 1000 grid. The $p(\text{class}_L|\phi, \mathcal{G})$ for each grid point ϕ are calculated and normalized to 1, as in Equation (3) (with the evaluated distribution $\boldsymbol{d}$ reduced to a single point ϕ)—i.e., the colors represent the probabilities of an event being classified as each class, if its parameters ϕ were exactly known. The black points in each panel are simulated events belonging to the corresponding classes. The None class is constructed to have probability density in regions of low- or zero-Galactic-model support. The WD and NS panels show that there are only relatively small or no regions where an event can have a high probability of being classified as such. In contrast, the star and SOBH panels show regions in the space where high-confidence lens classifications can be made.

(ϕ|None) to the bin centers, where

$$p(\phi|\ \text{None},\ \mathcal{G}) = A\left(1 - \frac{p(\phi|\mathcal{G})}{\max_\phi(p(\phi|\mathcal{G}))}\right) \tag{7}$$

and A is a constant that normalizes the probability density function to unity over the entire subspace. We assign the prior probability of the None class $p(\text{None}) = 0.01$. This class is then included as one of the classes in the set of classes in Section 3.2. Figure 2 shows the relative class probabilities in $\log_{10}t_{\rm E} - \log_{10}\pi_{\rm E}$ space, including the None class. Comparing Figures 1 and 2 shows that the None class is highest in regions of low- and zero-Galactic-model support. Figure 10 shows the effect of adding the None class on the tails of the WD class probability distribution.

This None class can also partially mitigate for a Galactic model that has an incomplete lens population, such as `PopSyCLE`. In the case of missing brown dwarfs and free-floating planet lenses, which can have largely nonoverlapping distributions in $\log_{10}t_{\rm E} - \log_{10}\pi_{\rm E}$ with the stellar distributions (i.e., $\log_{10}t_{\rm E} < 0.5$), the None class will absorb the event posterior density in those regions and the classifier will return a large None-class probability.

Overall, the None class described in this section traces the amount of posterior density an event has in a region of low- or zero-Galactic-population support. Events with high None-class probabilities should be treated with caution and generally investigated further.

For additional lens classes that are not included in the Galactic model but that overlap with the bulk of the simulation distribution (e.g., binary systems; N. S. Abrams et al. 2025a), the None class is not effective, as it has very small probability density in these regions by definition (see Equation (7)). To mitigate against this type of Galactic model uncertainty, the resulting classifications from many different Galactic models can be compared or averaged over. In this paper, we focus on different IFMRs that are likely to affect black hole classification probabilities. We make this classification framework available via the `popclass` Python package.[9]

3.4. Astrometric Posterior Predictive Distributions

In addition to lens classification, this framework can be used to derive posterior predictive distributions. In this work, we focus on photometric events and their subsequent astrometric follow-up in the context of SOBHs. For high-probability SOBH candidates, it is useful to be able to predict whether an event is likely to have a detectable astrometric signal if the lens is indeed an SOBH, so expensive astrometric follow-up observations can be allocated efficiently. This motivates predicting the angular scale of the event $\theta_{\rm E}$. This extension could also be used in the future for any other posterior predictive distributions of interest, such as lens masses or relative proper motions (allowing for selections of events where the luminous lens can be resolved from the source).

We can take the posterior constraints on the *photometric* microlensing parameters (e.g., $t_{\rm E}$ and $\pi_{\rm E}$) and, using the Galactic model, predict distributions on the parameters consistent with, but not directly constrained by, the light curve, such as $\theta_{\rm E}$. The posterior predictive density on $\theta_{\rm E}$ is then directly related to the predicted maximum possible astrometric deviation $\delta_{\rm max}$, which occurs at lens–source separation of $\sqrt{2}\,\theta_{\rm E}$ (M. Dominik & K. C. Sahu 2000):

$$\delta_{\rm max} = \frac{\sqrt{2}}{4}\theta_{\rm E}. \tag{8}$$

[9] https://github.com/LLNL/popclass

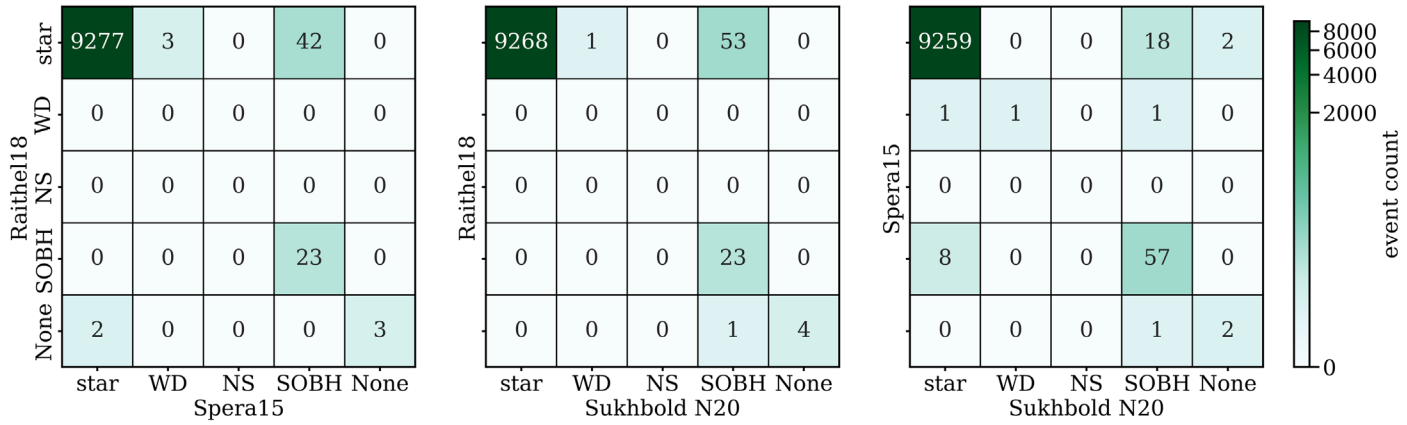

Figure 3. Pairwise confusion matrices between classifications based on three different Galactic models differing only in their IFMRs: Sukhbold N20 (based on models from T. Sukhbold & S. E. Woosley 2014; T. Sukhbold et al. 2016; S. E. Woosley 2017, 2020), Spera15 (M. Spera et al. 2015), and Raithel18 (C. A. Raithel et al. 2018). For a given Galactic model, the lens class is assigned as the class with the highest posterior probability. Events appearing along the diagonal mean that two different Galactic models agree on the lens classification. All IFMRs agree on bulk of the events being classified as stars. The right panel shows that Sukhbold N20 and Spera15 agree on the most SOBH lens classifications (57). The left and middle panels show that Raithel18 classifies most (42/53) events as stars that were assigned as SOBH candidates in the other (Spera15/Sukhbold N20) IFMRs. The 23 events for which Raithel18 agrees with the other IFMRs are the same in the left and middle panels, constituting our golden sample of SOBH candidates. See Section 4.1 for discussion.

The posterior predictive distribution on $\theta_{\rm E}$ given the light-curve data, $\boldsymbol{d}$, and Galactic model, $\mathcal{G}$, is

$$\begin{aligned} &p(\theta_{\rm E}|\mathcal{G}, \boldsymbol{d}, \text{class}_L = \text{SOBH}) \\ &\quad = \int p(\theta_{\rm E}, \phi|\mathcal{G}, \boldsymbol{d}, \text{class}_L = \text{SOBH}) \boldsymbol{d}\phi \,, \\ &\quad = \int \frac{p(\boldsymbol{d}|\phi) p(\theta_{\rm E}, \phi|\mathcal{G}, \text{class}_L = \text{SOBH})}{p(\boldsymbol{d}|\mathcal{G}, \text{class}_L = \text{SOBH})} \boldsymbol{d}\phi \,, \end{aligned} \tag{9}$$

where ϕ represents the photometric microlensing parameters. Note that the likelihood $p(\boldsymbol{d}|\phi)$ is independent of $\theta_{\rm E}$, as $\boldsymbol{d}$ represents the photometric data. This calculation compares the event's photometric likelihood to the expected distribution from a population model. While the mapping is not fully specified to translate the photometric parameters to $\theta_{\rm E}$, enfolding restrictions from the population model restricts the $\theta_{\rm E}$ space, which is still consistent with the photometric likelihood.

To sample the posterior predictive distribution for a high-probability SOBH candidate, we estimate $p(\theta_{\rm E}, \phi|\mathcal{G}, \text{class}_L = \text{SOBH})$ by building a 3D KDE over the Galactic simulation samples in the $\log_{10} t_{\rm E} - \log_{10} \pi_{\rm E} - \theta_{\rm E}$ space. Assuming our golden-sample candidates are in fact black holes, we now set out to assess their observed signals and chances for detection. We infer the $\theta_{\rm E}$ distribution for each candidate, using a 3D $\log_{10} t_{\rm E} - \log_{10} \pi_{\rm E} - \theta_{\rm E}$ KDE constructed on all simulated SOBH events from the Sukhbold N20 run and following Section 3.4. While there is no prior in Equation (9), as this is a predictive distribution and not a posterior distribution, we define a uniform prior in θ_E, because `dynesty` requires one and a uniform prior does not alter the results. We define a $\mathcal{U}(-2, 15 \quad [\text{mas}])$ prior for $\theta_{\rm E}$, allowing for a small margin of unphysical negative $\theta_{\rm E}$ to capture noisy distributions around near-zero values. We use the dynamic nested sampling algorithm (E. Higson et al. 2019) implemented by J. S. Speagle (2020) in the `dynesty` code. We use random walk sampling (J. Skilling et al. 2006) with multiple bounding ellipsoids and 1000 initial live points. We allocate samples with 100% of the weight placed on the posterior and use the default stopping function.

To compute the integral in Equation (9), we use the S independent posterior distribution samples from the photometric analysis and the importance-sampling technique described in Section 3, which gives

$$\begin{aligned} &p(\theta_{\rm E}|\mathcal{G}, \boldsymbol{d}, \text{class}_L = \text{SOBH}) \\ &\quad \propto \frac{1}{S} \sum_i^S \frac{p(\theta_{\rm E}, \hat{\phi}_i|\mathcal{G}, \text{class}_L = \text{SOBH})}{\pi(\hat{\phi}_i)} \,, \end{aligned} \tag{10}$$

$$\hat{\phi}_i \sim p(\phi_i|\boldsymbol{d}). \tag{11}$$

$\pi(\phi)$ denotes the prior density function used in modeling the events; here, for $\log_{10} t_{\rm E}$ and $\log_{10} \pi_{\rm E}$, it is a truncated normal distribution that can be found in Table 1 of N. Golovich et al. (2022).

4. Classification Results

4.1. High-probability Black Hole Candidates

We classify the event sample with three different Galactic models only differing in their underlying IFMRs: Sukhbold N20 (based on models from T. Sukhbold & S. E. Woosley 2014; T. Sukhbold et al. 2016; S. E. Woosley 2017, 2020), Spera15 (M. Spera et al. 2015), and Raithel18 (C. A. Raithel et al. 2018). A detailed description of all the IFMRs and their integration into the `PopSyCLE` simulation is provided in S. Rose et al. (2022). For each event and each IFMR, we assign a class corresponding to the highest $p(\text{class}_a|\boldsymbol{d}, \mathcal{G})$ value. We summarize those classifications in confusion matrices between pairs of IFMRs in Figure 3.

We find that while the three different IFMRs agree on classifying the majority of lenses as stars, the SOBH classifications are impacted by the underlying IFMR. The Raithel18 models yields significantly less black hole candidates than the other two, only finding 23 common SOBHs with Sukhbold N20 and Spera15. This is in contrast to Spera15 and Sukhbold N20, which agree on 57 SOBH candidates.

The reasons for this might be twofold. First, the Raithel18 simulation simply generates fewer black hole lenses; the prior black hole lens probability is equal to 0.0083 (as compared to 0.0100 and 0.0116 with the Spera15 and Sukhbold N20

Table 2
Overview of the 23 Black Hole Candidates

OGLE ID	α (deg)	δ (deg)	$\log_{10}(t_E\ [d])$	$\log_{10}\pi_E$	b_{sff}	$p(\mathrm{SOBH}\,\vert\boldsymbol{d},\,\mathcal{G}_{SN\,20})$
BLG117.1.89360	267.51625	−35.61075	$2.166^{+0.058}_{-0.055}$	$-1.50^{+0.32}_{-0.35}$	$0.036^{+0.006}_{-0.005}$	0.864
BLG131.1.104549	267.41833	−34.43564	$2.132^{+0.134}_{-0.062}$	$-1.38^{+0.30}_{-0.38}$	$0.614^{+0.336}_{-0.368}$	0.793
BLG195.1.373	268.42996	−29.52431	$2.180^{+0.081}_{-0.046}$	$-1.33^{+0.34}_{-0.39}$	$0.719^{+0.258}_{-0.348}$	0.797
BLG196.5.68751	270.84188	−29.25872	$2.077^{+0.012}_{-0.010}$	$-1.64^{+0.48}_{-0.45}$	$0.566^{+0.025}_{-0.028}$	0.788
BLG208.3.222797	271.59067	−28.74619	$1.858^{+0.008}_{-0.008}$	$-1.62^{+0.31}_{-0.34}$	$0.590^{+0.013}_{-0.013}$	0.428
BLG216.2.201174	270.74992	−28.29794	$1.992^{+0.042}_{-0.030}$	$-1.48^{+0.31}_{-0.36}$	$0.771^{+0.171}_{-0.181}$	0.641
BLG233.3.73254	270.74750	−27.06481	$2.177^{+0.062}_{-0.060}$	$-1.39^{+0.30}_{-0.31}$	$0.474^{+0.178}_{-0.119}$	0.860
BLG503.16.64872	267.16775	−34.85408	$2.299^{+0.074}_{-0.076}$	$-1.32^{+0.31}_{-0.39}$	$0.023^{+0.005}_{-0.005}$	0.767
BLG507.31.122188	269.01404	−31.13247	$2.097^{+0.027}_{-0.021}$	°	$0.851^{+0.142}_{-0.157}$	0.793
BLG515.15.27802	270.33738	−32.36358	$2.284^{+0.097}_{-0.052}$	$-1.48^{+0.28}_{-0.36}$	$1.399^{+0.567}_{-0.620}$	0.888
BLG518.30.17228	271.98604	-26.30169	$2.325^{+0.053}_{-0.050}$	$-1.55^{+0.37}_{-0.36}$	$0.627^{+0.126}_{-0.109}$	0.837
BLG520.10.64977	272.51396	−29.35044	$2.270^{+0.042}_{-0.057}$	$-1.35^{+0.48}_{-0.42}$	$0.207^{+0.069}_{-0.039}$	0.748
BLG580.12.77934	272.12962	−25.60019	$2.185^{+0.085}_{-0.082}$	$-1.38^{+0.32}_{-0.36}$	$0.347^{+0.130}_{-0.091}$	0.830
BLG605.20.76630	266.52504	−36.58792	$2.352^{+0.091}_{-0.067}$	$-1.17^{+0.38}_{-0.44}$	$1.484^{+0.542}_{-0.688}$	0.545
BLG632.18.118008	266.89000	−23.18578	$2.140^{+0.084}_{-0.046}$	$-1.34^{+0.30}_{-0.38}$	$1.332^{+0.453}_{-0.575}$	0.797
BLG632.20.147708	266.50442	−23.33761	$2.168^{+0.070}_{-0.061}$	$-1.62^{+0.28}_{-0.34}$	$0.588^{+0.281}_{-0.192}$	0.911
BLG633.25.85822	265.70662	−24.61531	$2.000^{+0.036}_{-0.028}$	$-1.46^{+0.30}_{-0.36}$	$0.943^{+0.189}_{-0.198}$	0.649
BLG638.18.94340	268.12804	−22.64825	$2.381^{+0.142}_{-0.118}$	$-1.22^{+0.26}_{-0.27}$	$0.161^{+0.104}_{-0.067}$	0.577
BLG643.28.35495	269.15404	−22.90167	$2.170^{+0.050}_{-0.032}$	$-1.30^{+0.22}_{-0.33}$	$1.047^{+0.200}_{-0.294}$	0.841
BLG645.26.75287	269.83983	−26.15864	$2.070^{+0.031}_{-0.029}$	$-1.57^{+0.37}_{-0.36}$	$0.749^{+0.172}_{-0.135}$	0.846
BLG652.18.94827	265.78996	−25.86931	$2.275^{+0.159}_{-0.074}$	$-1.35^{+0.31}_{-0.38}$	$0.829^{+0.550}_{-0.518}$	0.794
BLG661.12.38593	264.95212	−33.81094	$2.248^{+0.040}_{-0.046}$	$-1.40^{+0.31}_{-0.33}$	$0.129^{+0.034}_{-0.021}$	0.878
BLG662.21.34275	262.55525	−30.24875	$2.146^{+0.041}_{-0.034}$	$-1.47^{+0.31}_{-0.29}$	$1.077^{+0.226}_{-0.206}$	0.906

Note. We present OGLE IDs (field number + star number) and coordinates, posterior distribution statistics for the timescale, parallax, and blending from the modeling of N. Golovich et al. (2022), and the classifier-reported probability of belonging to the SOBH class under the Sukhbold N20 IFMR. The $\log_{10}(t_E\ [d])$, $\log_{10}\pi_E$, and b_{sff} distributions are represented as median values with 16th–84th percentile intervals. This table is a subset of the full classification results; the probabilities for all classes, all IFMRs, and all events will be made available in the online supplementary material.

(This table is available in its entirety in machine-readable form in the online article.)

simulation outputs, respectively). Second, the simulated Raithel18 black hole lenses are significantly less massive (on average $9.3M_\odot$, compared to $12.6M_\odot$ for Spera15 and $12.2M_\odot$ for Sukhbold N20); this may cause the population to be less well separated from non-SOBHs in $\log_{10} t_E - \log_{10}\pi_E$ space. Our observations reflect those of S. Rose et al. (2022), who note that the Raithel18 IFMR only produces black holes in the $5–16M_\odot$ range, while the other two include significantly higher masses. S. Rose et al. (2022) attribute the difference to the Raithel18 IFMR assuming solar metallicity for all progenitors, hence missing the most massive stellar remnants formed from the low-metallicity population.

We define the best black hole candidates as events that were assigned the SOBH class in classifications based on all three IFMRs. We give an overview of the 23 found candidates in Figure 4 and Table 2. This table is a subset of rows and columns from the full classification results table, where we report the probabilities for each class under each IFMR for each event; due to the size of the full table, we will publish it as an auxiliary data set upon acceptance of this paper.

We find that the inferred θ_E probability distribution is bimodal for all candidates. We present all θ_E distributions in Figure 5. We estimate the probability that the astrometric signal of an event could be detected by Hubble Space Telescope–like or Roman Space Telescope–like follow-up, assuming criteria of $\delta_{max} > 1$ mas and >0.1 mas, respectively, and checking the fraction of θ_E samples for the event passing these criteria.

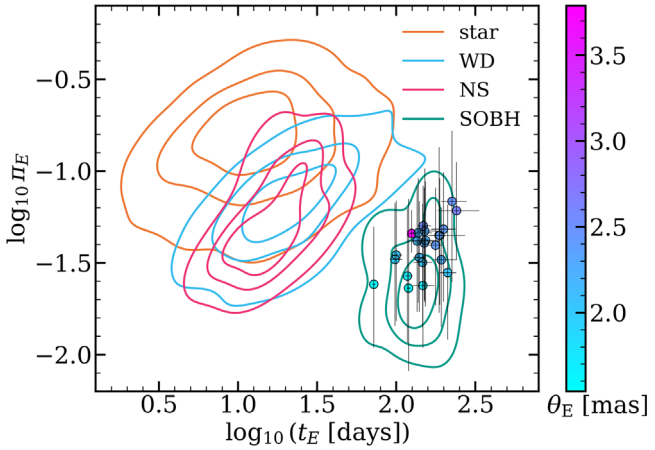

Figure 4. The 23 black hole candidates found in this work presented in $\log_{10}t_E$–$\log_{10}\pi_E$ space. The error bars indicate the 16th–84th percentiles of all posterior samples. The colors correspond to the median θ_E from the nested sampling posteriors. The isocontours (as in Figure 1) represent the KDEs of all astrophysical classes in the simulation output using the T. Sukhbold et al. (2016) IFMR.

To illustrate the expected signal, we simulate astrometric tracks for the best candidate, BLG507.31.122188, which has the highest probability of detectable signal—77%—and a b_{sff} (the ratio of flux coming from the source to the total observed flux) of $0.851^{+0.142}_{-0.157}$. Due to the source/total flux ratio being consistent with 1 (at 1.05σ), and keeping in mind the higher

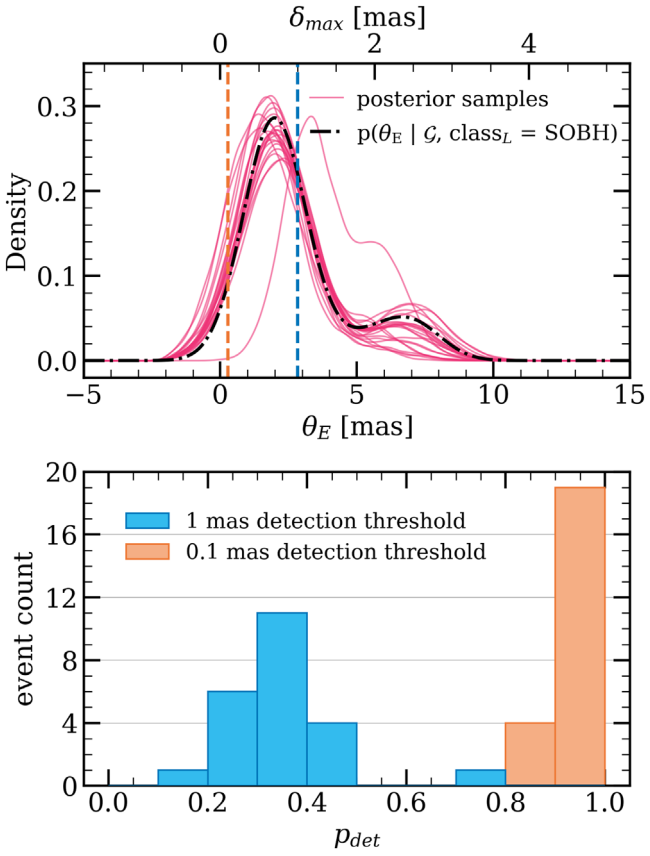

Figure 5. Top: posterior predictive θ_E distributions with the corresponding maximum astrometric deviation δ_{max} from nested sampling for all 23 strong SOBH candidates (represented as 10,000 posterior samples smoothed with a 1D Gaussian KDE). The vertical dashed blue line represents the precision of the Hubble Space Telescope–like astrometric follow-up (σ_{obs} = 1 mas), while the respective orange line represents that of the upcoming Roman Space Telescope–like follow-up (σ_{obs} = 0.1 mas). The dashed–dotted black line represents the prior predictive distribution $p(\theta_E|\mathcal{G}, \text{class}_L = \text{SOBH})$ constructed from the simulated events. Bottom: a histogram of the probability of detection of astrometric signals from the candidates given 1 mas (blue) or 0.1 mas (orange) detection thresholds, allocated at optimal times (including the peak astrometric signal and after the event), estimated as $p_{det} = p(\delta_{max} > \sigma_{obs})$ and integrated over all posterior samples for each event.

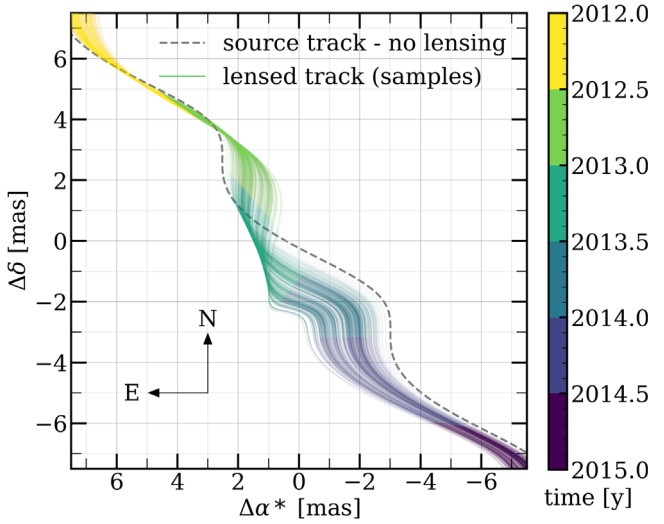

Figure 6. Simulated possible astrometric tracks for the black hole candidate BLG507.31.122188, which would be the most likely to have a detectable astrometric signal were follow-up observations to be allocated. The solid lines represent 300 randomly drawn θ_E values from posterior samples, while the dotted line represents the source track. The color-coding represents time in 0.5 yr intervals. The scale is centered so that the straight-line source motion is at (0, 0) during the event maximum ($t_0 = 2013.43$); $\Delta\delta$ represents the deviation from this position in δ; and $\Delta\alpha^*$ represents the deviation in $\alpha \cos\delta$. 1 mas—the fine grid-point separation—corresponds to the typical astrometric precision of Hubble Space Telescope observations or the along-scan precision of Gaia observations at $G \approx 18$ mag (the event brightness out of amplification).

spatial resolution of Gaia compared to OGLE, we assume this event to be unblended in Gaia. We match this candidate with a Gaia source of magnitude $G = 18.00$ and an available five-parameter astrometric solution; we assume Gaia observations should not be highly impacted by the lensing signal, as the event peaked in mid 2013 with a t_E of 125 days. The source motion is then defined by the five-parameter solution reported by Gaia, comprising the coordinates (α, δ), proper-motion components in their respective directions ($\mu_{\alpha*}$, μ_δ), and parallax π. We fix the photometric lensing parameters (t_0, u_0, t_E, π_E, ϕ) at their median values from modeling; finally, we sample the remaining parameter θ_E from the posterior predictive distribution. We draw 300 θ_E values from posterior samples and use the `astromet`[10] package to plot the simulated tracks in Figure 6.

As the events analyzed in this work happened between 2002 and 2017, it is not possible to schedule follow-up for an independent astrometric θ_E measurement. However, for some of the OGLE-IV events (spanning 2010–2017), there might be archival astrometric Gaia data. The Gaia mission (Gaia Collaboration et al. 2016) has been collecting data since 2014 July and is scheduled to operate until 2025. The next data release, Gaia DR4, will include astrometric time series from the first 5.5 yr of observations.

Even before the publication of the time-series data, indications from Gaia astrometric fits can be used to identify astrometric microlensing effects, estimate masses, and determine the nature of the lens (M. Jablonska et al. 2022). This is possible in cases of events with the most prominent astrometric signals (optimally, bright events with high Einstein radii, where the angular scale $\theta_E \gg$ the astrometric measurement error); "bad" fits indicating signals inconsistent with five-parameter motion can then be exploited to infer the magnitude of the astrometric deviation.

To vet our data set for possible events where this analysis could be done, we crossmatch the best SOBH candidate sample with the Gaia DR3 catalog (Gaia Collaboration et al. 2023). Out of the 23 events, 21 have a match (using a 1″ circle around the OGLE coordinates) in Gaia DR3 data, including 18 with astrometric fit parameters. The incomplete match is likely to be tied to lensing events typically occuring in crowded regions, where the Gaia completeness is significantly lower (e.g., T. Cantat-Gaudin et al. 2023). We find eight events for which the median $t_0 + t_E$ is larger than the start time of the Gaia observations, i.e., they are at least partially covered by Gaia; seven of them have a Gaia match.

Astrometry is significantly less likely to contain useful information and more difficult to analyze if events are blended. We use the criterion of a b_{sff} consistent with 1 (within 3σ, using a Gaussian fit to posterior samples) to further constrain the sample. This is a rough selection cut: blending is rarely well constrained in the modeling, as it is highly degenerate with other photometric parameters, such as u_0. Therefore, even for

[10] https://github.com/zpenoyre/astromet.py

Table 3
The Sample of Four SOBH Candidate Events Passing Basic Cuts for Possible Gaia Signal

OGLE ID	$t_{0,50}$ (yr)	RUWE	$\bar{G}_{\rm obs}$ (mag)	$\sigma_{\rm AL}(\bar{G}_{\rm obs})$ (mas)	$G_{\uparrow,\rm obs}$ (mag)	$\sigma_{\rm AL}(G_{\uparrow,\rm obs})$ (mas)	$G_{\uparrow,\rm pred}$ (mag)	$\sigma_{\rm AL}(G_{\uparrow,\rm pred})$ (mas)	$\delta_{\rm max}$ (mas)
BLG645.26.75287	2014.94	1.00	18.22	1.35	17.63	0.95	16.91	0.63	$0.62^{+0.49}_{-0.44}$
BLG662.21.34275	2016.80	1.18	19.73	3.95	18.47	1.61	18.36	1.49	$0.75^{+0.53}_{-0.45}$
BLG515.15.27802	2015.76	⋯	19.82	4.21	⋯	⋯	19.34	2.91	$0.79^{+0.68}_{-0.48}$
BLG605.20.76630	2014.51	⋯	20.71	8.08	⋯	⋯	20.43	6.57	$0.87^{+1.26}_{-0.52}$

Note. The median posterior of t_0, $t_{0,50}$ is given for reference, to situate events in the Gaia mission timeline. RUWE is the astrometric renormalized unit weight error; events with missing RUWE also have missing astrometric solutions. $\bar{G}_{\rm obs}$ stands for the `phot_g_mean_mag` column in the Gaia DR3 source catalog. $\sigma_{\rm AL}(\bar{G}_{\rm obs})$ is the along-scan astrometric error per single CCD transit corresponding to the $\bar{G}_{\rm obs}$ magnitude. For sources where DR3 time-series photometry is public (source catalog variability flag = `VARIABLE`), the brightest observed G value is reported as $G_{\uparrow,\rm obs}$ and the corresponding astrometric error is reported as $\sigma_{\rm AL}(G_{\uparrow,\rm obs})$. To estimate the expected precision for all events, a lower limit on the magnitude and astrometric error is calculated, assuming (optimistically) the magnitude at baseline = $\bar{G}_{\rm obs}$ and the magnitude at the peak, $G_{\uparrow,\rm pred}$, corresponding to its amplification at $u = u_{0,50}$—the posterior median of u_0. Events are sorted by increasing $\sigma_{\rm AL}(G_{\uparrow,\rm pred})$. All $\sigma_{\rm AL}$ values have been calculated with the `astromet` package. $\delta_{\rm max}$ is an estimate of the expected astrometric signal—the median value of the maximum astrometric deviation from posterior $\theta_{\rm E}$ samples with 16th–84th percentile intervals. Events with $\delta_{\rm max} > \sigma_{\rm AL}$ would be good candidates for detectable signals in time-series astrometry.

the events with a $b_{\rm sff}$ consistent with 1, some solutions with significant blending are allowed. On the other hand, events blended in OGLE do not necessarily have to be blended in Gaia; not only are the observations done in different bands, but also, most importantly, Gaia's spatial resolution is significantly higher. As anomalous astrometry during amplification can be caused by changing the weights in a blended light center of the source and the blend (e.g., Z. Kaczmarek et al. 2022), and could be misinterpreted as microlensing signal, we choose to keep this criterion, as a middle ground. As we make our classifications public, crossmatches with more relaxed or strict criteria can be made in the future.

The blending cut rejects three events, which have $b_{\rm sff}$ with median values of 0.02–0.16 and relatively well-constrained distributions ($0.005 \leqslant \sigma_{b_{\rm sff}} \leqslant 0.01$), indicating the blend to be significantly more luminous than the source. We analyze the possible astrometric signals of the remaining four candidates and present the results in Table 3.

We conclude there is no clear candidate for astrometric signal observable in Gaia. As all four found events are relatively faint in the G band, the expected astrometric signal is similar to or lower than the noise level. We also find no indication of excess astrometric signal beyond the five-parameter fits in the renormalized unit weight error (RUWE) values. In the literature, RUWE values between 1.25 (Z. Penoyre et al. 2022) and 1.4 (L. Lindegren 2018; L. Lindegren et al. 2021; P. Kervella et al. 2022) have typically been applied as a cutoff between well-behaved and anomalous (most often binary) sources; A. Castro-Ginard et al. (2024) have recently proposed a sky-variable RUWE threshold between 1.15 and 1.37, with the highest values occurring near the Galactic center. In light of those studies, none of our candidates pass the cut for anomalous motion based on RUWE alone. This does not exclude astrometric signal altogether but indicates that the astrometric solution is consistent with a five-parameter single-star motion. We suggest the Table 3 events should be revisited in the upcoming Gaia DR4 time-series data.

4.2. Fast Black Hole Probability Approximation

Figure 7 shows that for the events with $p(\,\mathrm{SOBH}\,|\boldsymbol{d},\,\mathcal{G}) > 0.2$, there is a high correlation between $\log_{10} t_{\rm E} - \log_{10}\pi_{\rm E}$, calculated with median posterior values, and $p(\,\mathrm{SOBH}\,|\boldsymbol{d},\,\mathcal{G})$. This allows a fast approximation of the probability that an event is caused by a black hole and could be useful in real-time data streams with a large volume of events, such as the Vera C. Rubin Observatory Legacy Survey of Space and Time (LSST).

We fit a straight line to all events with $\log_{10} t_{\rm E} - \log_{10}\pi_{\rm E} > 3$ for the median parameter values from posterior samples and average over all IFMR choices to obtain the relation

$$p(\mathrm{SOBH}|x)\begin{cases} <0.08 & \text{for} \quad x \leqslant 3 \\ \approx 0.930x - 2.713 & \text{for } 3 < x \leqslant 3.99. \\ \approx 1 & \text{for} \quad x > 3.99 \end{cases} \tag{12}$$

Here, $x = \log_{10} t_{\rm E} - \log_{10}\pi_{\rm E}$. This high correlation can be understood by examining the form of x and its dependence on M_L (via Equations (1) and (2)):

$$\log_{10}\left(\frac{t_{\rm E}}{\pi_{\rm E}}\right) = \log_{10}\left(\frac{\kappa M_{\rm L}}{\mu_{\rm rel}}\right). \tag{13}$$

Here, $\kappa = 8.144\,\mathrm{mas}/M_\odot$ and $\mu_{\rm rel}$ is the relative lens–source proper motion. Equation (13) shows that this variable is no longer dependent on D_S and within the logarithm is $\propto M_L$ compared with $t_{\rm E} \propto \sqrt{M_L}$. This stronger dependence on M_L allows better discrimination for high-mass lenses such as SOBHs. The effectiveness of x can also be understood in terms of the directions in $t_{\rm E} - \pi_{\rm E}$ space shown in Figure 1. x increases diagonally downward and to the right in $t_{\rm E} - \pi_{\rm E}$ space, which is the direction in which lens classes are separated.

4.3. Comparison with `DarkLensCode`

For the set of high-probability candidates found in Section 4.1, we compare the lens classification method in this paper to `DarkLensCode`[11] (K. Howil et al. 2025). While `DarkLensCode` is not able to classify an event as being caused by a black hole, it can estimate lens masses, distances, and the probability of the lens being dark. This method has both overlapping (i.e., black hole lenses should be dark) and complementary (i.e., lens mass and distances) information to our classification method.

We use the default `DarkLensCode` mass function, assign weight = 0 to samples with $M_{\rm lens} > 1000 M_\odot$, and sample for 10^6 iterations. Where possible, we use Gaia source proper-

[11] https://github.com/BHTOM-Team/DarkLensCode

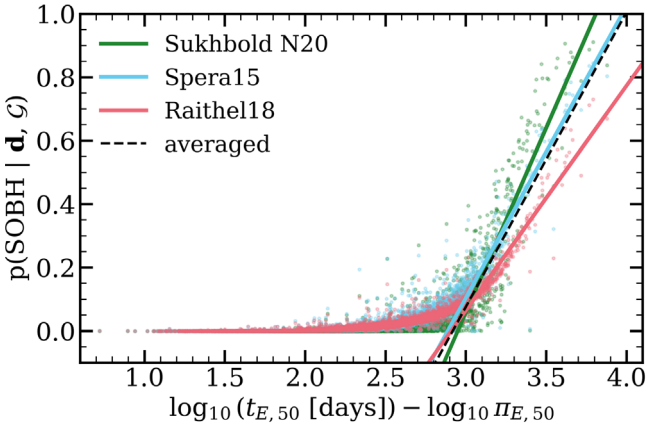

Figure 7. Fast approximation of the probability of the lens being an SOBH. The colors represent the three IFMRs used. The points represent all OGLE-III and OGLE-IV events: the X-axis position is defined as $x = \log_{10} t_{\rm E} - \log_{10} \pi_{\rm E}$ for the median parameter values from posterior samples (denoted with the subscript "50"), while the Y-axis position is the probability of belonging to the "SOBH" class from the classifier using a given IFMR. The solid straight lines represent the fast p(SOBH) estimation for each IFMR. The black dashed line represents the p(SOBH) estimation, averaging over all IFMRs (Equation (12)). For all IFMRs, p(SOBH) is strongly correlated with $\log_{10} t_{\rm E} - \log_{10} \pi_{\rm E}$, though the slope of the relationship varies, with the C. A. Raithel et al. (2018) IFMR in particular returning significantly lower p(SOBH) values.

motion and distance information. We take care to avoid contamination from the blend or astrometric lensing. In particular, where spectrophotometric distances (`distance_gspphot` in the Gaia source table) are available and $b_{\rm sff}$ is consistent with 1 (using the same criterion as in the Gaia crossmatch in Section 4.1), we use them along with their upper/lower bounds; otherwise, we sample from the `DarkLensCode` Galactic model within a range between 0 and 12 kpc for source distances. Where proper motions are available, if $b_{\rm sff}$ is consistent with 1 (again to avoid issues related to blending) and the maximum approach occurred at least $2t_{\rm E}$ before the start of Gaia observations (to avoid the influence of astrometric signals), we use the Gaia values; otherwise, we sample from the Galactic model. Where available, we use the OGLE-III I-band extinction calculator[12] (D. M. Nataf et al. 2013). For events without nearby extinction grid points (five out of 23 SOBH candidates) we use I-band values from the E. F. Schlafly & D. P. Finkbeiner (2011) extinction maps as implemented in the NASA/IPAC Extragalactic Database (NED) Extinction Calculator.[13] We find the `DarkLensCode` runtimes to be highly variable, depending on the auxiliary information provided, varying from ∼10 s to ∼10 minutes per event.

We find dark-lens probabilities between 97% and 100% for all events, regardless of the completeness of the Gaia source information. We also find relatively high masses, with median values between 13 and 91 $M_\odot$—all significantly more massive than the only isolated SOBH found so far (C. Y. Lam et al. 2022a) and overall closer to the most massive SOBH discovered so far in our Galaxy, GaiaBH 3 (Gaia Collaboration et al. 2024). Most lenses are situated on the near side of the bulge, between 6 and 8 kpc away. The two outlying (<2 kpc) candidates had available Gaia spectrophotometric distances that imposed strong constraints on the source being nearby. We present the inferred masses, distances, and dark-lens probabilities in Figure 8.

We also compare the inferred Einstein radii $\theta_{\rm E}$ and find that `DarkLensCode` predicts higher (on average by 62%) values; we present this comparison in Figure 8. This discrepancy can be explained as a consequence of the method. Both our inference and `DarkLensCode` use the limited information on $\theta_{\rm E}$ provided by photometric data and fill in the missing information using their respective Galactic model assumptions. In our inference, the missing information is provided directly in the $\theta_{\rm E}$ prior constructed from a simulated population of lenses. Contrarily, `DarkLensCode` uses dynamical information to infer $\theta_{\rm E}$, deriving it as $\theta_{\rm E} := t_{\rm E}\mu_{\rm rel}$. The $\mu_{\rm rel}$ values are sampled from a $\mathcal{U}(0, 30)$ (milliarcseconds per year) prior and evaluated using a simple model of disk and bulge velocity distributions, thus allowing loosely constrained high $\theta_{\rm E}$ values (i.e., there are no specific priors or constraints on the lens mass). Both methods have their strengths, as our inference is incorporating the full extent of information from the Galactic model, whereas `DarkLensCode` will perform better on unpredicted lens types, e.g., intermediate-mass black holes.

5. Classification of OB110462

In addition to the set of OGLE-IV microlensing events in the low-cadence fields, we apply our classification method to the only known microlensing event caused by an isolated black hole—OGLE-2011-BLG-0462, hereafter OB110462 (C. Y. Lam et al. 2022a; K. C. Sahu et al. 2022; C. Y. Lam & J. R. Lu 2023). As this work is focused on classifying microlensing events and selecting follow-up candidates based on photometry, we only use photometric data for this classification. We find that OB110462 has a posterior probability of being an SOBH, based on its photometric microlensing signal ranging between p(SOBH) = 0.049 and 0.224, depending on the Galactic model IFMR choice. The reason for this is that the $t_{\rm E} - \pi_{\rm E}$ posterior distribution for OB110462 is more consistent with the WD population (see Figure 9).

In the absence of astrometric microlensing data, one may use measurements of $t_{\rm E}$ and $\pi_{\rm E}$, along with a Galactic-model-based assumption for proper motion, to break the mass–distance degeneracy of a photometric microlensing event. Thus, several SOBH candidates have been identified based on high $t_{\rm E}$ and high $\pi_{\rm E}$ (e.g., D. P. Bennett et al. 2002; S. Poindexter et al. 2005; Ł. Wyrzykowski et al. 2016). The first astrometric microlensing follow-up programs primarily selected events from their long timescales alone, including, e.g., HST Program 12322, which began monitoring OB110462, and J. R. Lu et al. (2016). C. Y. Lam et al. (2020) showed via `PopSyCLE` that events with high $t_{\rm E}$ and low $\pi_{\rm E}$ are the best SOBH candidates in the direction of the Galactic bulge. Prior studies targeting or including high-$t_{\rm E}$, high-$\pi_{\rm E}$ candidates focused on a region of parameter space not well populated by `PopSyCLE` simulations and thus were likely biased toward outliers that could come from any of the populations.

There are several possible interpretations for the low SOBH class probability of OB110462. First, we could have just gotten lucky with this particular candidate. Although the posterior class probability of being an SOBH is low, it is still on average ≈14 times the prior probability of ≈0.01, according to the Galactic models (4.9, 27.0, and 9.2 times for the Spera15,

[12] https://ogle.astrouw.edu.pl/cgi-ogle/getext.py

[13] https://ned.ipac.caltech.edu/extinction_calculator. The NED is funded by the National Aeronautics and Space Administration and operated by the California Institute of Technology.

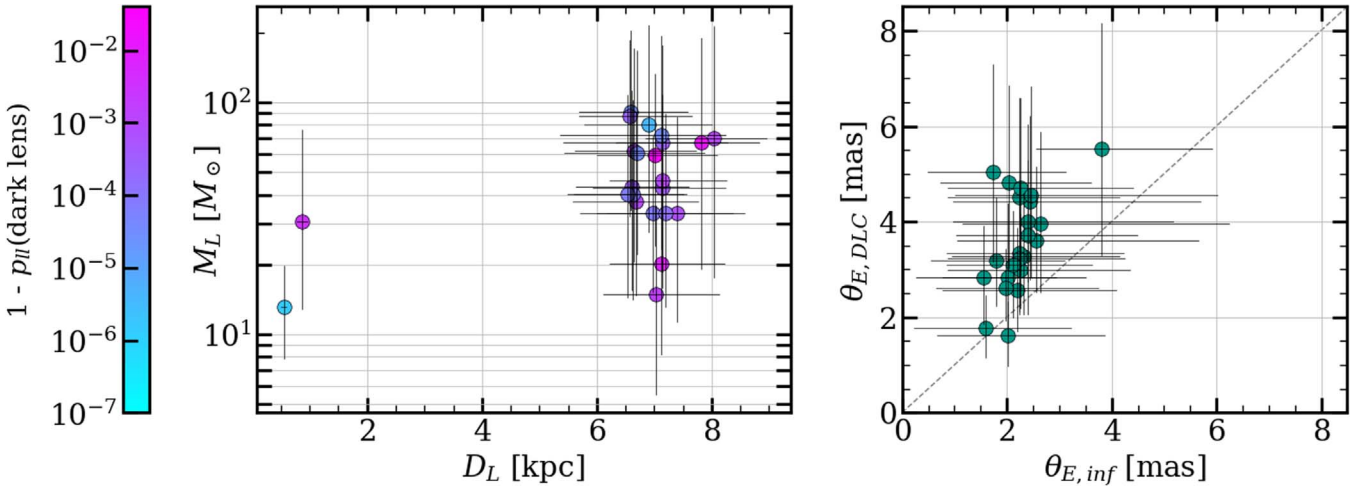

Figure 8. Results of `DarkLensCode` runs for the 23 strong SOBH candidates. Left: lens masses and distances returned by `DarkLensCode`, colored by 1 – the dark-lens probability (lower limit). According to the `DarkLensCode` results, all candidates have >97% dark-lens probability and high (13–91 $M_\odot$) masses; most candidates reside on the near side of the Galactic bulge, with the exception of two nearby lenses at distances within 0.5–1 kpc. Right: θ_E inferred from the `PopSyCLE` simulation results and nested sampling (see Section 3.4) vs. θ_E returned as `DarkLensCode` output. The error bars indicate the 16th–84th percentiles of samples. The $\theta_{E,inf}$ values cluster around 2 mas, where the prior distribution from the `PopSyCLE` simulation peaks, whereas the $\theta_{E,DLC}$ values are subject to less model constraints and are on average higher.

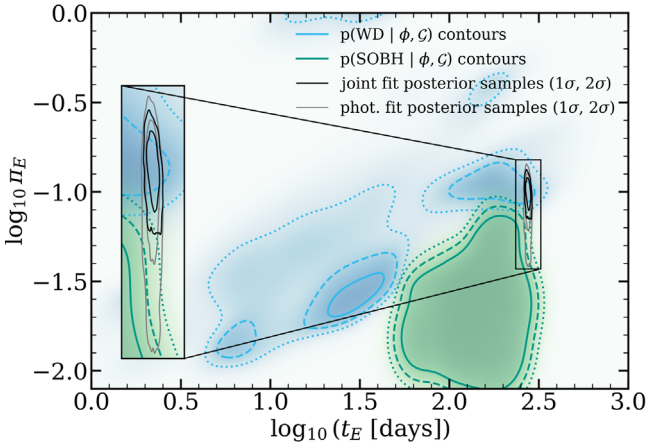

Figure 9. Classification of the only currently known isolated SOBH, OB110462 (C. Y. Lam et al. 2022a; K. C. Sahu et al. 2022). The background colors correspond to the subplots of Figure 2 for the WD and SOBH classes (using the T. Sukhbold et al. 2016 IFMR), overlaid with 50% opacity each. The contours mark $p(\text{class}_L|\phi, \mathcal{G}) = 0.3,\ 0.5,\ 0.7$ with the dotted, dashed, and solid lines, respectively; the color-coding of class_L is as in Figure 1 and thereafter. The solid contours enclose 68% and 95% of the posterior samples from the modeling of OB110462 from C. Y. Lam & J. R. Lu (2023). The gray contours represent the photometry-only fit, which was used for the classification; the black contours represent the joint fit using photometry and astrometry together, which further constrained the parameters. The inset shows the posterior sample distribution zoomed by a factor of 2.5. OB110462 is situated in the region of parameter space close to simulated events from both the WD and the SOBH class and showing steep gradients of $p(\text{class}_L|\phi, \mathcal{G})$.

Raithel18, and Sukhbold N20 IFMRs, respectively). This means that light-curve data do boost the chances of this event being caused by an SOBH lens. Moreover, this event was one of a set of five events in a similar region of $t_E - \pi_E$ space that were astrometrically followed up; the other four were ultimately found not to be SOBHs (e.g., C. Y. Lam et al. 2022b).

Second, the low SOBH probability of OB110462 may suggest that the underlying Galactic models on which the classifier is based are not quite correct. Each of these Galactic models comes with its own set of assumptions (SOBH abundance, Galactic structure, etc.), which, if changed, could shift the populations of SOBHs and WDs in $t_E - \pi_E$ space and consequently change the SOBH class probability of this event.

If the underlying Galactic models in our classifier are correct, then OB110462 is in the tails of the SOBH distribution and outlying in $t_E - \pi_E$ space. Regardless of the specific interpretation of OB110462's low SOBH class probability, it is an observational outlier—either it is an atypical SOBH, and the community got lucky finding it, or it is within the astrophysical SOBH distribution but outlying from expectations of current Galactic models. This interpretation is supported by N. Koshimoto et al. (2024), who also identified OB110462 as an outlier and used it to place constraints on the average SOBH progenitor kick distribution to be $\lesssim$100 km s^{-1}.

6. Discussion and Conclusion

We have developed and tested a new method of classifying microlensing events. Our method is effective in searching for black hole candidates, as black holes are well separated in $\log_{10}t_E$–$\log_{10}\pi_E$ space. We make a microlensing event population classifier using our methodology publicly available in the `popclass`[14] software package (G. Sallaberry et al. 2024).

The method is flexible, as the underlying Galactic model can be freely modified and new lens populations (e.g., primordial black holes and free-floating planets) can be added. The `popclass` documentation[15] contains instructions on how to extend and apply the methods described in this paper with a custom Galactic model simulation. It also requires no additional information beyond the t_E and π_E posteriors (we note it is not necessary to have a *detectable* parallax signal, and an upper constraint is sufficient for classification). This makes the method easy to apply to large data sets, as demonstrated in this study with the classification of ∼10,000 OGLE-III and OGLE-IV events. In combination with being fast (∼1 s for 10,000 posterior samples), lightweight, and conceptually

[14] https://github.com/LLNL/popclass
[15] https://popclass.readthedocs.io

simple, this makes the method ideal for integrating into real-time processing and alerting pipelines of variability surveys.

Another advantage is not relying on the source flux fraction $b_{\rm sff}$. Most prospective fields for microlensing searches are crowded; recognizing that a significant fraction of sources in those fields may have added light from close neighbors regardless of lensing, our method does not discard events with low $b_{\rm sff}$. Finally, as demonstrated in Section 3.4, the method can also be used to estimate $\theta_{\rm E}$ and the expected astrometric signal, which is especially useful in making decisions for allocating follow-up at $\sim$1 mas precision.

We also note the limitations of our method. First, it is more difficult to identify other classes of dark remnants in $\log_{10}t_{\rm E}$–$\log_{10}\pi_{\rm E}$ space alone; in particular, it is virtually impossible to identify high-probability NS candidates (see Figure 2). If those are the objects of interest, other event parameters should be used. For example, extending the parameter space to three dimensions (by adding astrometric information—$\theta_{\rm E}$) might be helpful, which will be possible on a large scale with the Roman Space Telescope.

As our method heavily relies on simulated events, it is only as good as the underlying Galactic model. This can be mitigated to some level with the None class, which identifies events in regions of low simulation support and may point toward missing physics. Still, it is not a fail-safe indicator of incompleteness in the case of overlapping populations. To minimize misclassifications, close connection between galaxy simulations and microlensing surveys should be maintained, and the simulations should be continuously updated. In this work, we use the current state-of-the-art software for simulations including dark remnants, `PopSyCLE`.

This classification method requires posterior samples of microlensing event parameters to be available as input. Although input posterior samples can be obtained by any method, this prerequisite is typically computationally expensive. The Markov Chain Monte Carlo (MCMC) inference in N. Golovich et al. (2022) took $\sim$100 CPU hours per event; this represents an extreme case where complex effects such as baseline variability were included. While typical point-source–point-lens MCMC modeling has lower ($\sim$minutes) runtimes, it still consumes significant resources compared to simpler optimization methods (e.g., E. Bachelet et al. 2017). Therefore, in cases of real-time classification, posterior samples would ideally be obtained in an automatic and fast way, using approximate methods such as simulation-based inference (e.g., K. Zhang et al. 2021) or Laplace approximation to posterior distributions (e.g., E. Bachelet et al. 2017). This classification method can also be readily applied to large databases of events with posterior distributions that have already been computed (e.g., N. Golovich et al. 2022; Z. Kaczmarek et al. 2022).

This classification method also assumes that the event under consideration is a genuine microlensing event, and it does not account for the possibility of contaminants in the event stream. Although variability surveys typically have dedicated pipelines for selecting microlensing events (e.g., M. S. Medford et al. 2023; Ł. Wyrzykowski et al. 2023), some false-positive microlensing events will pass and will be incorrectly classified by this method. However, in some cases, contaminants may have a high probability of being assigned to the "None" class, as they will have fitted microlensing parameters untypical for any astrophysical class (e.g., long-period variables having long-timescale but also highly asymmetric signal).

Finally, some events may have extra information that is helpful in classifying them, e.g., spectroscopic or kinematic information about the source. This method does not include such information, which is a trade-off to maximize simplicity and universality.

For the reasons outlined above, we conclude that this method is complementary to existing methods. Our classifier is well positioned to work as an initial filter, picking out the best black hole candidates from a large data set and optimizing the allocation of follow-up resources. Those candidates can then be treated on an individual basis, including adding auxiliary information.

We applied this method to search for black hole candidates in OGLE-III and OGLE-IV data. We found 23 events that we classified as strong black hole candidates, i.e., more likely to be a black hole than any other class regardless of the IMFR used. As all those events are archival and happened between 2002 and 2017, the possibility for analysis is limited. Some of our candidates have Gaia data collected during amplification and can be revisited in the time-series data set of the upcoming Gaia Data Release 4. Analysis with the `DarkLensCode` software ascribes very high (>97%) probabilities of being a dark remnant and high (13–91 $M_{\odot}$) masses to all of our strong black hole candidates. We also predict $\theta_{\rm E}$ from the posterior predictive distribution and the expected astrometric signal. Based on this method, we could have made follow-up decisions to observe candidates most likely to be detected astrometrically. We note that a fast reaction to follow up at the moment of highest astrometric deviation ($u = \sqrt{2}$) may be prioritized over having a maximally precise event posterior (return to baseline), as astrometric signals from the black hole candidates even at maximum are expected to be on the verge of current detection possibilities.

We find that the black hole classifications in particular are heavily impacted by the underlying IFMR, with the Raithel18 simulation run yielding significantly less black hole candidates than the other two. This also strongly limits the size of our black hole candidate sample. Future surveys such as the Roman Space Telescope will populate the $\log_{10}t_{\rm E} - \log_{10}\pi_{\rm E}$ space with tightly constrained data points. By working backward from lensing event parameter distributions, IFMRs can be constrained, and the underlying models of stellar evolution and supernova physics can be verified. This will be effective especially if the astrophysical class label is available independently, e.g., from astrometric mass measurement.

Looking forward, we anticipate an interesting and intense time for microlensing. Some ongoing astrometric microlensing SOBH searches have recently begun to focus on high-$t_{\rm E}$, low-$\pi_{\rm E}$ candidates (e.g., JWST DD Program 6777) and should have higher chances of success, in addition to providing valuable insights into this selection method's effectiveness and the accuracy of the underlying Galactic model. The increasing yield of events will make it critical to classify them in the most efficient way with minimal human intervention. The LSST at the Vera C. Rubin Observatory, which will detect thousands of photometric microlensing events over a wide field with high-cadence observations, presents an ideal case for this classifier, which could be integrated into target and observation managers (e.g., R. A. Street et al. 2018; S. van der Walt et al. 2019; D. A. Coulter et al. 2022, 2023) and applied automatically to all candidates labeled as microlensing. The classifier can also be applied to Roman Space Telescope data, with a possible

extension to three dimensions with astrometry. Applying our method to the upcoming large microlensing-event data sets may yield a substantial sample of isolated SOBHs and answer long-standing questions about this elusive population.

Acknowledgments

We thank George Chapline and Simeon Bird for many useful discussions on this work. We also thank Casey Lam for the photometric posterior distributions of OB110462. This work was performed under the auspices of the U.S. Department of Energy by Lawrence Livermore National Laboratory under Contract DE-AC52-07NA27344. The document number is LLNL-JRNL-870480. This work was supported by the LLNL-LDRD Program under Project 22-ERD-037. This document has been prepared as an account of work sponsored by an agency of the United States government. Neither the United States government nor Lawrence Livermore National Security, LLC, nor any of their employees, make any warranty, expressed or implied, or assume any legal liability or responsibility for the accuracy, completeness, or usefulness of any information, apparatus, product, or process disclosed, or represent that its use would not infringe privately owned rights. Reference herein to any specific commercial product, process, or service by trade name, trademark, manufacturer, or otherwise does not necessarily constitute or imply its endorsement, recommendation, or favoring by the United States government or Lawrence Livermore National Security, LLC. Z.K. acknowledges support from the 2024 LLNL Data Science Summer Institute and is a Fellow of the International Max Planck Research School for Astronomy and Cosmic Physics at the University of Heidelberg (IMPRS-HD). N.S.A., M.J.H., and J.R.L. acknowledge support from the National Science Foundation under grant No. 1909641 and the Heising–Simons Foundation under grant No. 2022-3542. M.F.H. was supported by a NASA FINESST grant No. ASTRO20-0022.

Software: This research has made use of NASA's Astrophysics Data System Bibliographic Services and `NumPy` (C. R. Harris et al. 2020), `SciPy` (P. Virtanen et al. 2020), `Matplotlib` (J. D. Hunter 2007), `Astropy` (Astropy Collaboration et al. 2013, 2018, 2022), `PopSyCLE` (C. Y. Lam et al. 2020), `Galaxia` (S. Sharma et al. 2011), `SPISEA` (M. W. Hosek et al. 2020), `scikit-learn` (F. Pedregosa et al. 2011), `dynesty` (J. S. Speagle 2020).

Appendix A
Comparison of Classifications with and without the None Class

In the additional Figure 10, we demonstrate an example of artificial regions of very high relative probability in parts of the parameter space not covered by simulated events. Had we not accounted for this effect, paradoxically, e.g., a lens classified as $p(\text{WD}\,|\boldsymbol{d}, \mathcal{G}) = 99\%$ should be treated as a less reliable WD candidate than a $p(\text{WD}\,|\boldsymbol{d}, \mathcal{G}) = 50\%$ one, as there are no WDs in the simulation output that would match its parameters. The simulation used in this figure uses the Spera15 IFMR, which exhibits especially striking ≈100% relative probability features in regions of no information before adding the None class. However, all simulation runs are affected.

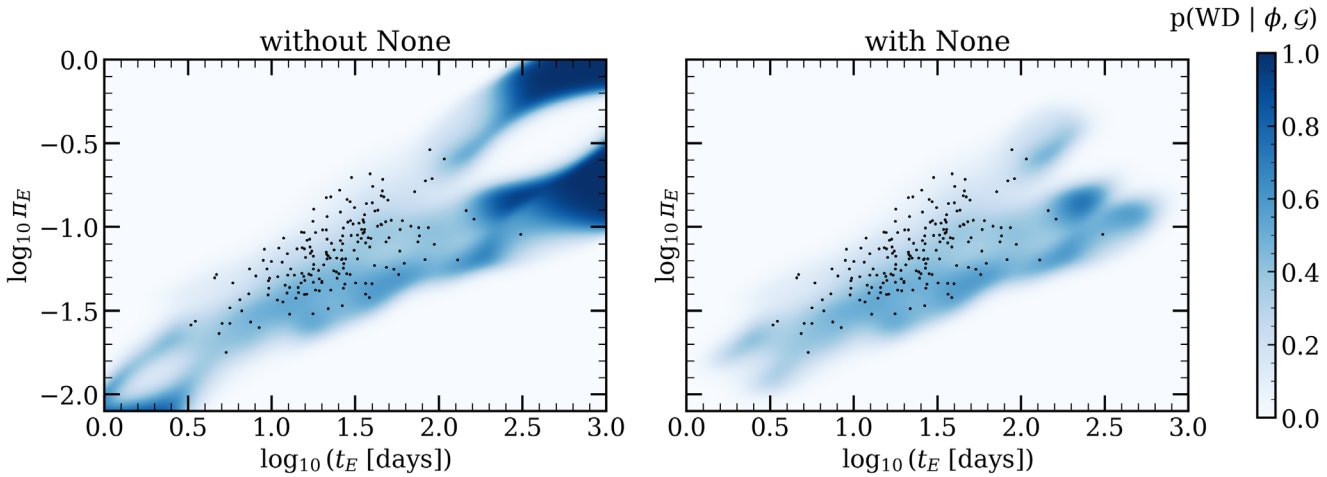

Figure 10. Relative classification probabilities for the WD class for points on a 1000 x 1000 grid, using the Spera15 IFMR, without (left) and with (right) the None class added to the classifier. The black points represent simulated events belonging to the class. The None class effectively erases the high-$p(\text{WD}\,|\phi, \mathcal{G})$ patterns in regions of low simulation support, leaving only those in proximity to simulated WD lens events.

Appendix B
Simulation Fields

In the additional Table 4, we provide an overview of the simulated survey fields used in this work and a breakdown of simulated event counts in each field (per astrophysical class and total).

Table 4
Event Counts in the 20 Simulated Fields

Field (l, b)	N(star)	N(WD)	N(NS)	N(SOBH)	$N_{\rm total}$
(−5.°6069, −2.°0233)	(46, 39, 36)	(7, 5, 6)	(0, 0, 1)	(2, 0, 0)	(55, 44, 43)
(−4.°2794, −5.°4419)	(31, 30, 20)	(4, 1, 3)	(1, 0, 3)	(0, 0, 1)	(36, 31, 27)
(−4.°2223, −6.°8055)	(5, 13, 3)	(1, 2, 2)	(1, 0, 0)	(0, 0, 0)	(7, 15, 5)
(−4.°2100, 4.°9609)	(26, 21, 27)	(3, 0, 3)	(0, 2, 1)	(0, 0, 1)	(29, 23, 32)
(−3.°2832, −3.°4735)	(91, 82, 76)	(11, 10, 17)	(0, 2, 1)	(3, 2, 1)	(105, 96, 95)
(−3.°2058, −4.°8329)	(58, 50, 58)	(8, 8, 4)	(1, 0, 1)	(0, 0, 0)	(67, 58, 63)
(−1.°9286, 1.°3682)	(42, 64, 50)	(3, 10, 6)	(0, 1, 0)	(0, 1, 0)	(45, 76, 56)
(−1.°0641, −3.°6101)	(130, 116, 114)	(22, 22, 20)	(0, 2, 3)	(0, 2, 1)	(152, 142, 138)
(−0.°9534, −6.°3377)	(34, 21, 26)	(4, 2, 3)	(0, 0, 1)	(0, 1, 0)	(38, 24, 30)
(0.°7819, 1.°6875)	(198, 190, 193)	(36, 29, 21)	(3, 3, 4)	(10, 3, 3)	(247, 225, 221)
(1.°1399, −3.°7432)	(229, 179, 150)	(23, 25, 24)	(2, 2, 1)	(3, 2, 4)	(257, 208, 179)
(3.°3316, −3.°8823)	(120, 118, 120)	(16, 13, 12)	(1, 4, 0)	(1, 2, 1)	(138, 137, 133)
(3.°5176, 3.°5577)	(66, 60, 61)	(9, 3, 6)	(0, 1, 0)	(1, 3, 1)	(76, 67, 68)
(3.°6341, 2.°1945)	(45, 57, 57)	(6, 8, 7)	(3, 1, 1)	(2, 1, 0)	(56, 67, 65)
(4.°4046, −3.°2761)	(84, 79, 68)	(8, 8, 10)	(0, 0, 1)	(1, 1, 2)	(93, 88, 81)
(4.°6747, 2.°8534)	(84, 86, 74)	(8, 6, 16)	(0, 2, 1)	(1, 1, 2)	(93, 95, 93)
(5.°4762, −2.°6684)	(46, 38, 38)	(3, 10, 4)	(1, 1, 1)	(1, 0, 0)	(51, 49, 43)
(5.°6025, 4.°8747)	(19, 14, 17)	(0, 2, 3)	(1, 1, 0)	(0, 0, 0)	(20, 17, 20)
(5.°8168, 2.°1491)	(49, 53, 46)	(9, 4, 8)	(0, 1, 1)	(1, 1, 0)	(59, 59, 55)
(6.°6383, −4.°8152)	(29, 24, 21)	(4, 2, 3)	(0, 1, 0)	(0, 0, 0)	(33, 27, 24)

Note. The first column shows the field center points (all fields are circles with an area of 0.3 deg^2). The following columns contain the numbers of events in the corresponding fields belonging to a given lens class in the Spera15, Raithel18, and Sukhbold N20 simulations, respectively.

ORCID iDs

Zofia Kaczmarek https://orcid.org/0009-0007-4089-5012
Peter McGill https://orcid.org/0000-0002-1052-6749
Scott E. Perkins https://orcid.org/0000-0002-5910-3114
William A. Dawson https://orcid.org/0000-0003-0248-6123
Macy Huston https://orcid.org/0000-0003-4591-3201
Ming-Feng Ho https://orcid.org/0000-0002-4457-890X
Natasha S. Abrams https://orcid.org/0000-0002-0287-3783
Jessica R. Lu https://orcid.org/0000-0001-9611-0009

References

Abbott, B. P., Abbott, R., Abbott, T. D., et al. 2016, PhRvX, 6, 041015
Abbott, B. P., Abbott, R., Abbott, T. D., et al. 2019, PhRvX, 9, 031040
Abbott, R., Abbott, T. D., Abraham, S., et al. 2021, PhRvX, 11, 021053
Abbott, R., Abbott, T. D., Acernese, F., et al. 2023, PhRvX, 13, 041039
Abbott, R., Abbott, T. D., Acernese, F., et al. 2024, PhRvD, 109, 022001
Abdurrahman, F. N., Stephens, H. F., & Lu, J. R. 2021, ApJ, 912, 146
Abrams, N. S., Hundertmark, M. P. G., Khakpash, S., et al. 2025b, ApJS, 276, 10
Abrams, N. S., Lu, J. R., Lam, C. Y., et al. 2025a, ApJ, 980, 103
Agol, E., & Kamionkowski, M. 2002, MNRAS, 334, 553
Agol, E., Kamionkowski, M., Koopmans, L. V. E., & Blandford, R. D. 2002, ApJL, 576, L131
Astropy Collaboration, Price-Whelan, A. M., Lim, P. L., et al. 2022, ApJ, 935, 167
Astropy Collaboration, Price-Whelan, A. M., Sipőcz, B. M., et al. 2018, AJ, 156, 123
Astropy Collaboration, Robitaille, T. P., Tollerud, E. J., et al. 2013, A&A, 558, A33
Bachelet, E., Hundertmark, M., & Calchi Novati, S. 2024, AJ, 168, 24
Bachelet, E., Norbury, M., Bozza, V., & Street, R. 2017, AJ, 154, 203
Barr, E. D., Dutta, A., Freire, P. C. C., et al. 2024, Sci, 383, 275
Belczynski, K., Wiktorowicz, G., Fryer, C. L., Holz, D. E., & Kalogera, V. 2012, ApJ, 757, 91
Bennett, D. P., Becker, A. C., Quinn, J. L., et al. 2002, ApJ, 579, 639
Bolton, C. T. 1972, Natur, 235, 271
Cantat-Gaudin, T., Fouesneau, M., Rix, H.-W., et al. 2023, A&A, 669, A55
Castro-Ginard, A., Penoyre, Z., Casey, A. R., et al. 2024, A&A, 688, A1
Coulter, D. A., Jones, D. O., McGill, P., et al. 2022, YSE-PZ: An Open-source Target and Observation Management System, v0.3.0, Zenodo, doi:10.5281/zenodo.7278430
Coulter, D. A., Jones, D. O., McGill, P., et al. 2023, PASP, 135, 064501
Damineli, A., Almeida, L. A., Blum, R. D., et al. 2016, MNRAS, 463, 2653
Dominik, M., & Sahu, K. C. 2000, ApJ, 534, 213
Dong, S., Mérand, A., Delplancke-Ströbele, F., et al. 2019, ApJ, 871, 70
El-Badry, K., Rix, H.-W., Cendes, Y., et al. 2023b, MNRAS, 521, 4323
El-Badry, K., Rix, H.-W., Quataert, E., et al. 2023a, MNRAS, 518, 1057
Fardeen, J., McGill, P., Perkins, S. E., et al. 2024, ApJ, 965, 138
Farr, W. M., Sravan, N., Cantrell, A., et al. 2011, ApJ, 741, 103
Gaia Collaboration, Panuzzo, P., Mazeh, T., et al. 2024, A&A, 686, L2
Gaia Collaboration, Prusti, T., de Bruijne, J., et al. 2016, A&A, 595, A1
Gaia Collaboration, Vallenari, A., Brown, A. G. A., et al. 2023, A&A, 674, A1
Gardner, J. P., Mather, J. C., Clampin, M., et al. 2006, SSRv, 123, 485
Golovich, N., Dawson, W., Bartolić, F., et al. 2022, ApJS, 260, 2
Gould, A. 1994, ApJL, 421, L71

Gould, A. 2004, ApJ, 606, 319
Harris, C. R., Millman, K. J., van der Walt, S. J., et al. 2020, Natur, 585, 357
Hearnshaw, J. B., Abe, F., Bond, I. A., et al. 2006, in 9th Asian-Pacific Regional IAU Meeting, ed. W. Sutantyo et al. (Bandung: Institut Teknologi Bandung Press), 272
Higson, E., Handley, W., Hobson, M., & Lasenby, A. 2019, Statistics and Computing, 29, 891
Ho, M. F., Perkins, S. E., Bird, S., et al. 2024, PhRvD, 110, 063031
Hog, E., Novikov, I. D., & Polnarev, A. G. 1995, A&A, 294, 287
Hosek, M. W., Jr., Lu, J. R., Lam, C. Y., et al. 2020, AJ, 160, 143
Howil, K., Wyrzykowski, Ł., Kruszyńska, K., et al. 2025, A&A, 694, A94
Hunter, J. D. 2007, CSE, 9, 90
Husseiniova, A., McGill, P., Smith, L. C., & Evans, N. W. 2021, MNRAS, 506, 2482
Ivezić, Ž., Kahn, S. M., Tyson, J. A., et al. 2019, ApJ, 873, 111
Jablonska, M., Wyrzykowski, L., Rybicki, K. A., et al. 2022, A&A, 666, L16
Johnson, S. A., Penny, M., Gaudi, B. S., et al. 2020, AJ, 160, 123
Kaczmarek, Z., McGill, P., Evans, N. W., et al. 2022, MNRAS, 514, 4845
Kaczmarek, Z., McGill, P., Evans, N. W., et al. 2024, MNRAS, 529, 1308
Kalirai, J. S., Hansen, B. M. S., Kelson, D. D., et al. 2008, ApJ, 676, 594
Kervella, P., Arenou, F., & Thévenin, F. 2022, A&A, 657, A7
Kim, S. L., Lee, C. U., Park, B. G., et al. 2016, JKAS, 49, 37
Klüter, J., Bastian, U., & Wambsganss, J. 2020, A&A, 640, A83
Koshimoto, N., Kawanaka, N., & Tsuna, D. 2024, ApJ, 973, 5
Kreidberg, L., Bailyn, C. D., Farr, W. M., & Kalogera, V. 2012, ApJ, 757, 36
Kruszyńska, K., Wyrzykowski, Ł., Rybicki, K. A., et al. 2024, A&A, 692, A28
Lam, C. Y., & Lu, J. R. 2023, ApJ, 955, 116
Lam, C. Y., Lu, J. R., Hosek, M. W., J., Dawson, W. A., & Golovich, N. R. 2020, ApJ, 889, 31
Lam, C. Y., Lu, J. R., Udalski, A., et al. 2022a, ApJL, 933, L23
Lam, C. Y., Lu, J. R., Udalski, A., et al. 2022b, ApJS, 260, 55
Lindegren, L. 2018, GAIA-C3-TN-LU-LL-124-01, http://www.rssd.esa.int/doc_fetch.php?id=3757412
Lindegren, L., Bastian, U., Biermann, M., et al. 2021, A&A, 649, A4
Lu, J. R., Sinukoff, E., Ofek, E. O., Udalski, A., & Kozlowski, S. 2016, ApJ, 830, 41
Mao, S., Smith, M. C., Woźniak, P., et al. 2002, MNRAS, 329, 349
McClintock, J. E., & Remillard, R. A. 2006, Compact Stellar X-ray Sources, Vol. 39 (Cambridge: Cambridge Univ. Press), 157
McGill, P., Anderson, J., Casertano, S., et al. 2023, MNRAS, 520, 259
McGill, P., Everall, A., Boubert, D., & Smith, L. C. 2020, MNRAS, 498, L6
McGill, P., Smith, L. C., Evans, N. W., Belokurov, V., & Lucas, P. W. 2019, MNRAS, 487, L7
McGill, P., Smith, L. C., Evans, N. W., Belokurov, V., & Smart, R. L. 2018, MNRAS, 478, L29
Medford, M. S., Abrams, N. S., Lu, J. R., Nugent, P., & Lam, C. Y. 2023, ApJ, 947, 24
Minniti, D., Lucas, P. W., Emerson, J. P., et al. 2010, NewA, 15, 433
Miyamoto, M., & Yoshii, Y. 1995, AJ, 110, 1427
Mróz, P., Udalski, A., Skowron, J., et al. 2019, ApJS, 244, 29
Mróz, P., Udalski, A., Szymański, M. K., et al. 2020, ApJS, 249, 16
Nataf, D. M., Gould, A., Fouqué, P., et al. 2013, ApJ, 769, 88
Pedregosa, F., Varoquaux, G., Gramfort, A., et al. 2011, JMLR, 12, 2825
Penny, M. T., Gaudi, B. S., Kerins, E., et al. 2019, ApJS, 241, 3
Penoyre, Z., Belokurov, V., & Evans, N. W. 2022, MNRAS, 513, 2437
Perkins, S. E., McGill, P., Dawson, W., et al. 2024, ApJ, 961, 179
Piffl, T., Scannapieco, C., Binney, J., et al. 2014, A&A, 562, A91
Poindexter, S., Afonso, C., Bennett, D. P., et al. 2005, ApJ, 633, 914
Pruett, K., Dawson, W., Medford, M. S., et al. 2024, ApJ, 970, 169
Raithel, C. A., Sukhbold, T., & Özel, F. 2018, ApJ, 856, 35
Remillard, R. A., & McClintock, J. E. 2006, ARA&A, 44, 49
Robin, A. C., Reylé, C., Derrière, S., & Picaud, S. 2004, A&A, 416, 157
Rose, S., Lam, C. Y., Lu, J. R., et al. 2022, ApJ, 941, 116
Rybicki, K. A., Shvartzvald, Y., Yee, J. C., et al. 2024, ApJ, 975, 216
Rybicki, K. A., Wyrzykowski, Ł., Klencki, J., et al. 2018, MNRAS, 476, 2013
Ryu, Y. H., Yee, J. C., Udalski, A., et al. 2018, AJ, 155, 40
Sahu, K. C., Anderson, J., Casertano, S., et al. 2017, Sci, 356, 1046
Sahu, K. C., Anderson, J., Casertano, S., et al. 2022, ApJ, 933, 83
Sallaberry, G., Kaczmarek, Z., McGill, P., et al. 2024, arXiv:2410.14076
Schlafly, E. F., & Finkbeiner, D. P. 2011, ApJ, 737, 103
Scott, D. W. 1992, Multivariate Density Estimation: Theory, Practice, and Visualization (New York, Chicester: John Wiley & Sons)
Shao, Y. 2022, RAA, 22, 122002
Sharma, S., Bland-Hawthorn, J., Johnston, K. V., & Binney, J. 2011, ApJ, 730, 3
Shin, I. G., Yee, J. C., Zang, W., et al. 2024, AJ, 167, 269
Shvartzvald, Y., Bryden, G., Gould, A., et al. 2017, AJ, 153, 61
Skilling, J., et al. 2006, BayAn, 1, 833
Smith, M. C., Belokurov, V., Evans, N. W., Mao, S., & An, J. H. 2005, MNRAS, 361, 128
Smith, M. C., Mao, S., & Paczyński, B. 2003, MNRAS, 339, 925
Speagle, J. S. 2020, MNRAS, 493, 3132
Spera, M., Mapelli, M., & Bressan, A. 2015, MNRAS, 451, 4086
Spergel, D., Gehrels, N., Baltay, C., et al. 2015, arXiv:1503.03757
Street, R. A., Bowman, M., Saunders, E. S., & Boroson, T. 2018, Proc. SPIE, 10707, 1070711
Sukhbold, T., Ertl, T., Woosley, S. E., Brown, J. M., & Janka, H. T. 2016, ApJ, 821, 38
Sukhbold, T., & Woosley, S. E. 2014, ApJ, 783, 10
Sumi, T., Bennett, D. P., Bond, I. A., et al. 2013, ApJ, 778, 150
Terry, S. K., Bennett, D. P., Bhattacharya, A., et al. 2022, AJ, 164, 217
Udalski, A. 2003, AcA, 53, 291
Udalski, A., Szymański, M. K., & Szymański, G. 2015, AcA, 65, 1
van der Walt, S., Crellin-Quick, A., & Bloom, J. 2019, JOSS, 4, 1247
Virtanen, P., Gommers, R., Oliphant, T. E., et al. 2020, NatMe, 17, 261
Walker, M. A. 1995, ApJ, 453, 37
Webster, B. L., & Murdin, P. 1972, Natur, 235, 37
Woosley, S. E. 2017, ApJ, 836, 244
Woosley, S. E., Sukhbold, T., & Janka, H. T. 2020, ApJ, 896, 56
Wyrzykowski, Ł., Kostrzewa-Rutkowska, Z., Skowron, J., et al. 2016, MNRAS, 458, 3012
Wyrzykowski, Ł., Kruszyńska, K., Rybicki, K. A., et al. 2023, A&A, 674, A23
Wyrzykowski, Ł., & Mandel, I. 2020, A&A, 636, A20
Wyrzykowski, Ł., Rynkiewicz, A. E., Skowron, J., et al. 2015, ApJS, 216, 12
Zhang, K., Bloom, J. S., Gaudi, B. S., et al. 2021, AJ, 161, 262